

Probing the CP nature of the Higgs bosons by $t\bar{t}$ production at photon linear colliders

Eri Asakawa^{a,b}, and Kaoru Hagiwara^b

^a *International Center for Elementary Particle Physics,
University of Tokyo, Tokyo 113-0033, Japan*

^b *Theory Group, KEK, Tsukuba, Ibaraki 305-0801, Japan*

Abstract

We study effects of heavy Higgs bosons on the $t\bar{t}$ production process at photon linear colliders. The interference patterns between the resonant Higgs-production amplitudes and the continuum QED amplitudes are examined. The patterns tell us not only the CP nature of the Higgs bosons but also the phase of the $\gamma\gamma$ -Higgs vertex which gives new information about the Higgs couplings to new charged particles. We point out that it is necessary to use circularly polarized photon beams to produce efficiently heavy Higgs bosons whose masses exceed the electron beam energy, and show that the above interference patterns of the production amplitudes can be studied by observing t and \bar{t} decay angular distributions. Analytic expressions for the helicity amplitudes for the sequential process $\gamma\gamma \rightarrow t\bar{t} \rightarrow (bW^+)(\bar{b}W^-) \rightarrow (bf_1\bar{f}_2)(\bar{b}f_3\bar{f}_4)$ are presented in terms of the generic $\gamma\gamma \rightarrow t\bar{t}$ production amplitudes.

1 Introduction

The scalar sector of the Standard Model (SM) consists of one $SU(2)_w$ doublet. After the electroweak symmetry breaking (EWSB), a neutral CP-even Higgs boson remains as a physical state. Although the SM is consistent with the current experimental data, new physics will be indispensable if we consider the hierarchy between the electroweak scale and the Planck scale, a failure of the gauge coupling unification etc. as serious problems. It is natural that new physics modify the mechanism of the EWSB. Such modification may lead to appearance of Higgs bosons with various CP properties. In the case that an extra doublet extends the scalar sector of the SM, extra two neutral and two charged Higgs bosons should be observed. If CP is a good symmetry of the scalar sector, one additional neutral boson is CP-even and the other is CP-odd. Therefore, probing the CP property as well as the masses, the decay widths and the couplings of all the Higgs bosons is necessary for exploring the Higgs sector.

One of colliders which can play an important role in studying the Higgs sector is a photon linear collider (PLC), an option of e^+e^- linear colliders [1, 2, 3]. The energy of the colliding photons, which are obtained by the backward Compton scattering of laser light on high-energy electrons, reaches about 80% of the energy of the original electron beam [4]. Since neutral Higgs bosons are produced as s -channel resonances via loops of charged massive particles, we can detect the Higgs bosons whose masses are less than about 80% of the collision energy of a parent e^+e^- collider. Thus, a PLC has a great advantage of detecting heavy neutral Higgs bosons whose masses exceed the reach of the LHC and an e^+e^- LC especially for those of the minimal supersymmetric SM (MSSM) [5]. For light Higgs bosons, it has been well known that the $\gamma\gamma$ decay widths of the Higgs bosons can be accurately measured [6]. The measurement is important because the contribution from heavy charged particles which couple to the Higgs bosons does not decouple from the vertex if their masses originate from the EWSB. As for CP nature of Higgs bosons, CP-even and

CP-odd Higgs bosons can be clearly distinguished by utilizing the linear polarization of colliding photons [7]. This powerful technique, however, is effective to probe the CP nature of relatively light Higgs bosons only, because the linear polarization transfer of the Compton back-scattered laser light decreases significantly when the photon energy is more than half the electron beam energy [4, 8]. For the heavier Higgs bosons whose masses exceed the electron beam energy, $t\bar{t}$ production process with circularly polarized photons is useful to study their CP properties [9, 10, 11].

In this paper, we revisit the study of the CP nature of neutral Higgs bosons through the $t\bar{t}$ production process at a PLC. Such study has been performed in [9], [10] and [11]. It has been shown in Sec. 4.4 of [9] that; if we observe sizable interference between the Higgs-resonant and QED-continuum amplitudes for the two helicity combinations of the top pairs produced by circularly polarized colliding photons, we can determine the CP parity of the Higgs bosons. In [10], the observables which are useful for complete determination of the $\gamma\gamma$ -Higgs and $t\bar{t}$ -Higgs couplings have been presented, in the presence of CP non-conserving interactions. The accuracy of the determination of those couplings has been studied in [11], by using the combined asymmetries involving the circular polarization of colliding photons and the charge of charged leptons in top decays with a cut off on the lepton angle.

In this paper, we extend the study of [9], and study the interference patterns of the resonant and the continuum amplitudes in more detail for the $\gamma\gamma \rightarrow t\bar{t}$ process by using the circularly polarized colliding photons. We find that not only the squares of the helicity amplitudes but also the real and imaginary parts of the interference between the two helicity amplitudes can be measured by studying the angular correlations of t and \bar{t} decay products. They are useful for deriving the information on the CP nature of Higgs bosons. It will also be shown that these interference effects allow us to observe the complex phase of the $\gamma\gamma$ -Higgs vertices.

This paper is organized as follows. In Sect. 2 helicity amplitudes for the process $\gamma\gamma \rightarrow t\bar{t}$ are given. In Sect. 3 observables which are sensitive to the CP-parity of the Higgs bosons as

well as the complex phase of the $\gamma\gamma$ -Higgs vertex are discussed. Numerical estimates of the observables which are introduced in Sect. 3 are performed in Sect. 4. We give conclusions in the last section. Analytic expressions for the helicity amplitudes for the sequential process $\gamma\gamma \rightarrow t\bar{t} \rightarrow (bW^+)(\bar{b}W^-) \rightarrow (bf_1\bar{f}_2)(\bar{b}f_3\bar{f}_4)$ are presented in appendix A.

2 Helicity amplitudes for the process $\gamma\gamma \rightarrow t\bar{t}$

When the $\gamma\gamma$ collision energy reaches around mass of a spinless boson ϕ ($\phi = H$ or A where H and A are the CP-even and CP-odd Higgs bosons respectively.), the process

$$\gamma(k_1, \lambda_1) + \gamma(k_2, \lambda_2) \rightarrow t(p, \sigma) + \bar{t}(\bar{p}, \bar{\sigma}) \quad (2.1)$$

receives leading contributions from the diagrams in which the spinless boson is exchanged in the s -channel and the top quark is exchanged in the t - and u -channels. The four-momenta and the helicities of the participating particles in the colliding $\gamma\gamma$ center-of-mass frame are given in parentheses. We adopt the notation [12] where the photon (fermion) helicities are denoted by the signs in units of \hbar ($\hbar/2$)¹. The helicity amplitudes of the process can be expressed as

$$\mathcal{M}_{\lambda_1\lambda_2}^{\sigma\bar{\sigma}} = [\mathcal{M}_\phi]_{\lambda_1\lambda_2}^{\sigma\bar{\sigma}} + [\mathcal{M}_t]_{\lambda_1\lambda_2}^{\sigma\bar{\sigma}}, \quad (2.2)$$

where the first term \mathcal{M}_ϕ stands for the s -channel ϕ -exchange amplitudes and the latter term \mathcal{M}_t stands for the t - and u -channel top-quark-exchange amplitudes. The resonant helicity amplitudes are calculated by using the lowest-dimensional effective Lagrangian of the form

$$\mathcal{L}_{\phi\gamma\gamma} = \frac{1}{m_\phi} \left(b_\gamma^H A_{\mu\nu} A^{\mu\nu} + b_\gamma^A \tilde{A}_{\mu\nu} A^{\mu\nu} \right) \phi, \quad (2.3)$$

$$\mathcal{L}_{\phi t\bar{t}} = \bar{t} \left(d_t^H + id_t^A \gamma_5 \right) t \phi, \quad (2.4)$$

¹For fermion helicities we often use the notation L and R instead of $-$ and $+$

where $A_{\mu\nu} = \partial_\mu A_\nu - \partial_\nu A_\mu$ and $\tilde{A}_{\mu\nu} = \frac{1}{2}\epsilon_{\mu\nu\rho\sigma}A^{\rho\sigma}$ (where $\epsilon_{0123} = 1$) are the photon field strength tensor and its dual tensor, respectively. The resonant amplitudes are then expressed as products of the $\gamma\gamma\phi$ vertex function $A_\phi^{\lambda_1\lambda_2}$, the Higgs propagator factor B_ϕ and the decay vertex $C_\phi^{\sigma\bar{\sigma}}$,

$$[\mathcal{M}_\phi]_{\lambda_1\lambda_2}^{\sigma\bar{\sigma}} = A_\phi^{\lambda_1\lambda_2} B_\phi C_\phi^{\sigma\bar{\sigma}} \quad (2.5)$$

where

$$A_\phi^{\lambda_1\lambda_2} = \left(b_\gamma^H + i\lambda_1 b_\gamma^A\right) \frac{\hat{s}}{m_\phi} \delta_{\lambda_1\lambda_2}, \quad (2.6)$$

$$B_\phi = \frac{1}{m_\phi^2 - \hat{s} - im_\phi\Gamma_\phi}, \quad (2.7)$$

$$C_\phi^{\sigma\bar{\sigma}} = \left(\beta \sigma d_t^H - id_t^A\right) \sqrt{\hat{s}} \delta_{\sigma\bar{\sigma}}. \quad (2.8)$$

In the CP-conserving limit, the H - and A -exchange amplitudes are [9]

$$[\mathcal{M}_H]_{\lambda_1\lambda_2}^{\sigma\bar{\sigma}} = \sigma \beta b_\gamma^H d_t^H \frac{\hat{s}}{m_H^2 - \hat{s} - im_H\Gamma_H} \frac{\sqrt{\hat{s}}}{m_H} \delta_{\lambda_1,\lambda_2} \delta_{\sigma,\bar{\sigma}}, \quad (2.9)$$

$$[\mathcal{M}_A]_{\lambda_1\lambda_2}^{\sigma\bar{\sigma}} = \lambda_1 b_\gamma^A d_t^A \frac{\hat{s}}{m_A^2 - \hat{s} - im_A\Gamma_A} \frac{\sqrt{\hat{s}}}{m_A} \delta_{\lambda_1,\lambda_2} \delta_{\sigma,\bar{\sigma}}, \quad (2.10)$$

where β is the velocity of the top quarks and \hat{s} is the total energy-squared in the rest frame of $\gamma\gamma$ collisions. The masses and the total decay widths of the Higgs bosons are denoted by m_ϕ and Γ_ϕ .

In the following, we sometimes use the predictions of the MSSM as examples. The effective couplings are expressed in the MSSM as

$$\begin{aligned} d_t^H &= -\frac{gm_t \sin \alpha}{2m_W \sin \beta}, \\ d_t^A &= \frac{gm_t}{2m_W} \cot \beta, \end{aligned} \quad (2.11)$$

for the ttH and ttA couplings, where g is the SU(2) gauge coupling, $\tan \beta = \langle v_u \rangle / \langle v_d \rangle$ is the ratio of the two Higgs vacuum expectation values, and α is the mixing angle between

the neutral real components of the two Higgs doublets and the two CP-even Higgs bosons. The $\gamma\gamma H$ and $\gamma\gamma A$ couplings are induced in the one loop level:

$$\begin{aligned} b_\gamma^H(\hat{s}) &= \frac{\alpha g m_H}{8\pi m_W} \sum_i I_H^i \left(\frac{\hat{s}}{m_i^2} \right), \\ b_\gamma^A(\hat{s}) &= -\frac{\alpha g m_A}{8\pi m_W} \sum_i I_A^i \left(\frac{\hat{s}}{m_i^2} \right). \end{aligned} \quad (2.12)$$

The dimensionless loop functions I_H^i and I_A^i for all the MSSM diagrams (labeled by the index i , where the masses of particles in the loops are expressed by m_i) are found e.g. in [13]. As long as the SUSY particles are heavier than the top quark, the top quark contribution dominates over all the other contributions. The effective couplings b_γ^H and b_γ^A are real when all the particles in the loops are heavy, and become complex above the thresholds.

The irreducible background to the resonant ϕ -production process is the non-resonant top-quark-exchange processes, whose amplitudes are expressed in the tree level of QED as [9]

$$\begin{aligned} [\mathcal{M}_t]_{\lambda_1\lambda_2}^{\sigma\bar{\sigma}} &= \frac{8\pi\alpha Q_t^2}{1 - \beta^2 \cos^2 \Theta} \times \\ &\{(\beta\sigma + \lambda_1)/\gamma \delta_{\lambda_1,\lambda_2} \delta_{\sigma,\bar{\sigma}} - \beta/\gamma \sigma \sin^2 \Theta \delta_{\lambda_1,-\lambda_2} \delta_{\sigma,\bar{\sigma}} \\ &- \beta(\sigma\lambda_1 + \cos \Theta) \sin \Theta \delta_{\lambda_1,-\lambda_2} \delta_{\sigma,-\bar{\sigma}}\}. \end{aligned} \quad (2.13)$$

Here $1/\gamma = \sqrt{1 - \beta^2} = 2m_t/\sqrt{\hat{s}}$ and Θ is the polar angle of the top-quark momentum in the colliding $\gamma\gamma$ c.o.m. frame. In Table 1, the amplitudes in units of the common factor $8\pi\alpha Q_t^2/(1 - \beta^2 \cos^2 \Theta)$ are summarized. In the table, the photon helicities $\lambda_1\lambda_2$ are given in the first column, and the $t\bar{t}$ helicities $\sigma\bar{\sigma}$ are denoted as RR, LL, RL, LR for $(\sigma\bar{\sigma}) = (++)$, $(--)$, $(+-)$, $(-+)$, respectively, in the first row. It should be noted that the four amplitudes in the left top column of Table 1, those for $\lambda_1 = \lambda_2$ and $\sigma = \bar{\sigma}$, interfere with the resonant amplitudes of eq. (2.5). Furthermore, at high energies ($\beta \rightarrow 1$, $\gamma \gg 1$) all the $\sigma = \bar{\sigma}$ amplitudes are suppressed by $1/\gamma$, among which the amplitudes for $\sigma = \bar{\sigma} = -\lambda = -\bar{\lambda}$ are suppressed by $1/\gamma^3$. These properties as well as the relative signs

of the top-quark-exchange amplitudes will be found useful in probing the CP nature of the Higgs bosons in the following sections.

Table 1: The tree-level helicity amplitudes of $\gamma\gamma \rightarrow t\bar{t}$, $[\mathcal{M}_t]_{\lambda_1\lambda_2}^{\sigma\bar{\sigma}}$, in eq. (2.13). The common factor $8\pi\alpha Q_t^2/(1 - \beta^2 \cos^2 \Theta)$ is omitted in the table. The two photon helicities $\lambda_1\lambda_2$ are given in the first column, and the $t\bar{t}$ helicities $\sigma\bar{\sigma}$ are denoted as RR , LL , RL , LR for $(\sigma\bar{\sigma}) = (++)$, $(--)$, $(+-)$, $(-+)$, respectively, in the first row.

	RR	LL	RL	LR
$++$	$(1 + \beta)/\gamma$	$(1 - \beta)/\gamma$	0	0
$--$	$-(1 - \beta)/\gamma$	$-(1 + \beta)/\gamma$	0	0
$+-$	$-\beta/\gamma \sin^2 \Theta$	$\beta/\gamma \sin^2 \Theta$	$-\beta \sin \Theta(1 + \cos \Theta)$	$\beta \sin \Theta(1 - \cos \Theta)$
$-+$	$-\beta/\gamma \sin^2 \Theta$	$\beta/\gamma \sin^2 \Theta$	$\beta \sin \Theta(1 - \cos \Theta)$	$-\beta \sin \Theta(1 + \cos \Theta)$

3 Determining the CP parity of the Higgs bosons

3.1 Overview

The helicity dependence of the amplitudes discussed in the previous section is summarized in Table 2. We note here that the individual (H -exchange, A -exchange, and t -exchange) amplitudes for the helicities $\lambda = \bar{\lambda} = -$ and $\lambda = \bar{\lambda} = -\sigma = -\bar{\sigma}$ are obtained from the $\lambda = \bar{\lambda} = \sigma = \bar{\sigma} = +$ amplitudes $[\mathcal{M}_{H,A,t}]_{++}^{++}$ by multiplying the appropriate sign-factor representing the CP transformation property and the kinematical factor for the top-quark-exchange amplitudes. Here $[\mathcal{M}_{H,A,t}]_{++}^{++}$ are denoted by $\mathcal{M}_{H,A,t}$ for simplicity. When the polarization of the colliding beams is fixed, e.g. as $\lambda = \bar{\lambda} = +$, the sign of the H -production amplitude changes when the helicities of final top pairs are flipped. On the other hand, the sign of the A -production amplitude does not depend on the helicities of final top pairs. The sign of the top-quark-exchange amplitudes does not depend on the $t\bar{t}$ helicities, just like the A -exchange amplitudes, but the amplitude is reduced by a factor of $(1 - \beta)/(1 + \beta) = 1/[\gamma^2(1 + \beta)^2]$ when the top-quark-helicity is opposite to

Table 2: The helicity dependence of the amplitudes of $\gamma(\lambda)\gamma(\lambda) \rightarrow t(\sigma)\bar{t}(\bar{\sigma})$, $[\mathcal{M}]_{\lambda\lambda}^{\sigma\bar{\sigma}}$. We denote $[\mathcal{M}]_{++}^{RR}$ as \mathcal{M} for \mathcal{M}_t , \mathcal{M}_H and \mathcal{M}_A , which denote the top-, H - and A -exchange amplitudes, respectively. The two photon helicities $\lambda\lambda$ are given in the first column, and the $t\bar{t}$ helicities $\sigma\bar{\sigma}$ are denoted as RR , LL for $(\sigma\bar{\sigma}) = (++)$, $(--)$, respectively, in the first row.

	RR	LL
++	\mathcal{M}_t \mathcal{M}_H \mathcal{M}_A	$\frac{1-\beta}{1+\beta}\mathcal{M}_t$ $-\mathcal{M}_H$ \mathcal{M}_A
--	$-\frac{1-\beta}{1+\beta}\mathcal{M}_t$ \mathcal{M}_H $-\mathcal{M}_A$	$-\mathcal{M}_t$ $-\mathcal{M}_H$ $-\mathcal{M}_A$

the photon helicity, $\lambda_1 = \lambda_2 = -\sigma = -\bar{\sigma}$. Therefore, the top-quark-helicity dependence of the interference pattern between the resonant amplitudes and the top-quark-exchange amplitudes can be used to determine the CP parity of the Higgs resonance [9]. It should further be noted that within the given helicity amplitude the interference pattern below and above the resonance is also a good probe the CP parity. In our phase connection, \mathcal{M}_t is positive at all \hat{s} , whereas the ϕ -exchange amplitude \mathcal{M}_ϕ is positive at low \hat{s} where the absorptive part of the $\phi\gamma\gamma$ vertex can be neglected for the dominant top-quark loop contribution. We should hence expect constructive interference below the resonance when $\lambda_1 = \lambda_2 = \sigma = \bar{\sigma}$. The above statements are valid for both H and A , or their arbitrary mixture when CP is violated. The interference pattern for the $\lambda_1 = \lambda_2 = -\sigma = -\bar{\sigma}$ amplitude is expected to reverse for H , whereas it remains the same for A . Both signs are possible when the resonance ϕ does not have a definite CP parity.

Based on the above observation, we study carefully the interference patterns between the helicity amplitudes, that receive contribution from the s -channel spin-0 resonance production. In general, four types of observables can be studied in the process $\gamma\gamma \rightarrow t\bar{t}$ where the initial photon polarization can be controlled by the backward Compton scattering of

the laser light and the $t\bar{t}$ polarization are measured through the angular distributions of the correlated cascade decays, $t \rightarrow bW^+ \rightarrow bf_1\bar{f}_2$ and $\bar{t} \rightarrow \bar{b}W^- \rightarrow \bar{b}f_3\bar{f}_4$. All the observables which are sensitive to the spin-0 resonance contributions are listed below;

- $|\mathcal{M}_{\lambda\lambda}^{RR}|^2, |\mathcal{M}_{\lambda\lambda}^{LL}|^2$ for $\lambda = +, -;$ (3.1)

- $\text{Re}, \text{Im}[\mathcal{M}_{\lambda\lambda}^{RR} (\mathcal{M}_{\lambda\lambda}^{LL})^*]$ for $\lambda = +, -;$ (3.2)

- $\text{Re}, \text{Im}[\mathcal{M}_{++}^{\sigma\sigma} (\mathcal{M}_{--}^{\sigma\sigma})^*]$ for $\sigma = R, L;$ (3.3)

- $\text{Re}, \text{Im}[\mathcal{M}_{++}^{\sigma\sigma} (\mathcal{M}_{--}^{-\sigma, -\sigma})^*]$ for $\sigma = R, L.$ (3.4)

The observables (3.1) have been studied in [9] and they are found to be useful in distinguishing A from H . The observables (3.3) have been studied in [10] and are found to be effective in probing the CP nature of the neutral Higgs sector, including the case of CP-violation. Unfortunately, the observables (3.3) require linear polarization of the colliding photon beams, whose magnitude is small for $z \equiv \sqrt{\hat{s}}/\sqrt{s} \gtrsim 0.5$ where \sqrt{s} is the c.o.m. energy of a parent e^-e^- collider [4, 8]. In this article, we concentrate on the observables (3.1) and (3.2), which can take advantage of the high $\gamma\gamma$ luminosity at large z with high level of monochromaticity, that are obtained from the backward Compton scattering of circularly polarized laser lights on longitudinally polarized electron beams. The CP-violating cases will be studied elsewhere [14]. To our knowledge, the observables of the type (3.4), whose observation requires both the linearly polarized photons and the angular correlations of t and \bar{t} decays, have not been studied.

3.2 Observables

Because the top quark polarizations are measured through its decay angular distribution [15, 16], we study the cascade process

$$\gamma(k_1, \lambda_1) + \gamma(k_2, \lambda_2) \rightarrow t(p, \sigma) + \bar{t}(\bar{p}, \bar{\sigma}) \quad (3.5)$$

$$\rightarrow b(p_b, L) W^+(p_W, \Lambda) + \bar{b}(\bar{p}_b, R) W^-(\bar{p}_W, \bar{\Lambda}) \quad (3.6)$$

$$\rightarrow b(p_b, L) f_1(p_1, L) \bar{f}_2(p_2, R) + \bar{b}(\bar{p}_b, R) f_3(p_3, L) \bar{f}_4(p_4, R) \quad (3.7)$$

where we assume the SM amplitudes for the decays, and neglect masses of all final fermions including b and \bar{b} . The helicity amplitudes for the full process (3.7), $\mathbf{M}_{\lambda_1\lambda_2}$, are given in appendix A. The differential cross section for arbitrary initial photon helicities

$$\begin{aligned} & \frac{d\hat{\sigma}_{\lambda_1\lambda_2}}{d \cos \Theta d \cos \theta d \phi d \cos \bar{\theta} d \bar{\phi} d \cos \theta^* d \phi^* d \cos \bar{\theta}^* d \bar{\phi}^*} \\ &= \frac{3\beta}{32\pi\hat{s}} \left| \mathbf{M}_{\lambda_1\lambda_2}(\Theta; \theta, \phi; \bar{\theta}, \bar{\phi}; \theta^*, \phi^*; \bar{\theta}^*, \bar{\phi}^*) \right|^2 \times B_{12}B_{34} \end{aligned} \quad (3.8)$$

is readily obtained in the zero-width limit of the top quarks and the W bosons. Here B_{12} is the branching fraction of $W^+ \rightarrow f_1\bar{f}_2$ decays, and B_{34} is that of $W^- \rightarrow f_3\bar{f}_4$, $\hat{s} = (k_1 + k_2)^2$ is the total-energy squared in the colliding $\gamma\gamma$ c.o.m. system, Θ is the polar angle of the top-quark momentum in this frame measured from the direction of the photon beam with the momentum k_1 , θ and ϕ ($\bar{\theta}$ and $\bar{\phi}$) are the polar and azimuthal angles, respectively, of the W^+ (W^-) momentum in the t (\bar{t}) rest-frame. The polar angles (θ and $\bar{\theta}$) are measured from the top-quark momentum direction in the $\gamma\gamma$ c.o.m. frame and the azimuthal angles (ϕ and $\bar{\phi}$) are measured from the $\gamma\gamma \rightarrow t\bar{t}$ scattering plane. Here we choose the common polar axis and the $\phi = \bar{\phi} = 0$ plane to describe the $t \rightarrow bW^+$ and $\bar{t} \rightarrow \bar{b}W^-$ decays, so that our coordinate frame for $\bar{t} \rightarrow \bar{b}W^-$ decays is obtained from the frame used for $t \rightarrow bW^+$ decays by a single boost along the top-quark momentum direction. Finally, θ^* and ϕ^* ($\bar{\theta}^*$ and $\bar{\phi}^*$) are the polar and azimuthal angles, respectively, of the \bar{f}_2 (f_3) momentum in the W^+ (W^-) rest-frame. The polar angle θ^* ($\bar{\theta}^*$) is measured from the W^+ (W^-) momentum direction in the t (\bar{t}) restframe, and the azimuthal angle ϕ^* ($\bar{\phi}^*$) is measured from the W^+b ($W^-\bar{b}$) decay plane in the $\gamma\gamma$ collision c.o.m. frame. The origins of the azimuthal angles are chosen such that the y-axis for $\phi = \bar{\phi} = \frac{\pi}{2}$ is along the $\vec{k}_1 \times \vec{p}$ direction in the $\gamma\gamma$ c.o.m. frame, that for $\phi^* = \frac{\pi}{2}$ ($\bar{\phi}^* = \frac{\pi}{2}$) is along the $\vec{p} \times \vec{p}_{W^+}$ ($\vec{p} \times \vec{p}_{W^-}$) direction also in the $\gamma\gamma$ c.o.m. frame.

If we assume that the top-quark decays are essentially described by the SM amplitudes as above, it is straightforward to extract all the four observables (3.1) and (3.2), for a given initial photon polarization ($\lambda_1 = \lambda_2 = +$ or $-$), by studying the t and \bar{t} decay angular distributions. Optimal accuracy of such measurements can readily be estimated by using the exclusive distributions [17] for a given range of the scattering angle Θ . Such measurements should be especially effective near the $t\bar{t}$ threshold where the Θ -dependence of the background amplitude is moderate. In this article, we present a primitive version of such analysis where we assume that the exclusive distributions of the $\gamma\gamma \rightarrow t\bar{t} \rightarrow bW^+\bar{b}W^-$ process (3.6) are measured for transverse and longitudinally polarized W 's (W_T and W_L , respectively) separately. We assume that the W^+ (W^-) helicity is measured in the t (\bar{t}) rest frame. Such distributions are in principle measurable when the W -pair decays hadronically or semi-leptonically. When both W 's decay leptonically, presence of two energetic neutrinos in the final state makes it impossible to reconstruct the W momenta uniquely. It should further be noted that W_T and W_L can be distinguished experimentally even when the W decays hadronically, though less efficiently than the leptonic-decay case.

The differential cross sections for polarized W 's are now expressed compactly as follows:

$$\frac{d\hat{\sigma}_{\lambda_1\lambda_2}^{\Lambda\bar{\Lambda}}}{d\cos\Theta d\cos\theta d\phi d\cos\bar{\theta} d\bar{\phi}} = \frac{3\beta}{32\pi\hat{s}} \left| \mathbf{M}_{\lambda_1\lambda_2}^{\Lambda\bar{\Lambda}}(\Theta; \theta, \phi, \bar{\theta}, \bar{\phi}) \right|^2. \quad (3.9)$$

Explicit forms of the helicity amplitude $\mathbf{M}_{\lambda_1\lambda_2}^{\Lambda\bar{\Lambda}}$ appear in appendix B. Here, we consider the case of $\lambda_1 = \lambda_2 = \lambda$, because high luminosity and high degree of polarization for energetic two photon pairs can be achieved at a PLC. The four relevant squared matrix elements for $\lambda_1 = \lambda_2 = \lambda$ are

$$\begin{aligned} |\mathbf{M}_{\lambda\lambda}^{LL}|^2 = \frac{B_L^2}{16\pi^2} \{ & |\mathcal{M}_{\lambda\lambda}^{RR}|^2(1 + \cos\theta)(1 + \cos\bar{\theta}) \\ & + |\mathcal{M}_{\lambda\lambda}^{LL}|^2(1 - \cos\theta)(1 - \cos\bar{\theta}) \\ & + 2 \operatorname{Re} \left[\mathcal{M}_{\lambda\lambda}^{RR} \cdot (\mathcal{M}_{\lambda\lambda}^{LL})^* \right] \sin\theta \sin\bar{\theta} \cos(\phi - \bar{\phi}) \\ & - 2 \operatorname{Im} \left[\mathcal{M}_{\lambda\lambda}^{RR} \cdot (\mathcal{M}_{\lambda\lambda}^{LL})^* \right] \sin\theta \sin\bar{\theta} \sin(\phi - \bar{\phi}) \}, \end{aligned} \quad (3.10)$$

$$|\mathbf{M}_{\lambda\lambda}^{LT}|^2 = \frac{B_L B_T}{16\pi^2} \left\{ |\mathcal{M}_{\lambda\lambda}^{RR}|^2 (1 + \cos\theta)(1 - \cos\bar{\theta}) \right. \quad (3.11)$$

$$+ |\mathcal{M}_{\lambda\lambda}^{LL}|^2 (1 - \cos\theta)(1 + \cos\bar{\theta}) \\ - 2 \operatorname{Re} [\mathcal{M}_{\lambda\lambda}^{RR} \cdot (\mathcal{M}_{\lambda\lambda}^{LL})^*] \sin\theta \sin\bar{\theta} \cos(\phi - \bar{\phi}) \\ + 2 \operatorname{Im} [\mathcal{M}_{\lambda\lambda}^{RR} \cdot (\mathcal{M}_{\lambda\lambda}^{LL})^*] \sin\theta \sin\bar{\theta} \sin(\phi - \bar{\phi}) \},$$

$$|\mathbf{M}_{\lambda\lambda}^{TL}|^2 = \frac{B_L B_T}{16\pi^2} \left\{ |\mathcal{M}_{\lambda\lambda}^{RR}|^2 (1 - \cos\theta)(1 + \cos\bar{\theta}) \right. \quad (3.12)$$

$$+ |\mathcal{M}_{\lambda\lambda}^{LL}|^2 (1 + \cos\theta)(1 - \cos\bar{\theta}) \\ - 2 \operatorname{Re} [\mathcal{M}_{\lambda\lambda}^{RR} \cdot (\mathcal{M}_{\lambda\lambda}^{LL})^*] \sin\theta \sin\bar{\theta} \cos(\phi - \bar{\phi}) \\ + 2 \operatorname{Im} [\mathcal{M}_{\lambda\lambda}^{RR} \cdot (\mathcal{M}_{\lambda\lambda}^{LL})^*] \sin\theta \sin\bar{\theta} \sin(\phi - \bar{\phi}) \},$$

$$|\mathbf{M}_{\lambda\lambda}^{TT}|^2 = \frac{B_T^2}{16\pi^2} \left\{ |\mathcal{M}_{\lambda\lambda}^{RR}|^2 (1 - \cos\theta)(1 - \cos\bar{\theta}) \right. \quad (3.13)$$

$$+ |\mathcal{M}_{\lambda\lambda}^{LL}|^2 (1 + \cos\theta)(1 + \cos\bar{\theta}) \\ + 2 \operatorname{Re} [\mathcal{M}_{\lambda\lambda}^{RR} \cdot (\mathcal{M}_{\lambda\lambda}^{LL})^*] \sin\theta \sin\bar{\theta} \cos(\phi - \bar{\phi}) \\ - 2 \operatorname{Im} [\mathcal{M}_{\lambda\lambda}^{RR} \cdot (\mathcal{M}_{\lambda\lambda}^{LL})^*] \sin\theta \sin\bar{\theta} \sin(\phi - \bar{\phi}) \},$$

where $B_L = m_t^2/(m_t^2 + 2m_W^2)$ and $B_T = 2m_W^2/(m_t^2 + 2m_W^2)$ are the branching ratios of the decays $t \rightarrow bW_L^+$ ($\bar{t} \rightarrow \bar{b}W_L^-$) and $t \rightarrow bW_T^+$ ($\bar{t} \rightarrow \bar{b}W_T^-$), respectively. It is clear that $|\mathcal{M}_{\lambda\lambda}^{RR}|^2$ and $|\mathcal{M}_{\lambda\lambda}^{LL}|^2$ are obtained by integrating out the $\phi - \bar{\phi}$ azimuthal angle distributions, and they can be distinguished by using the W^+ and W^- polar angle (θ and $\bar{\theta}$) distributions. Since it is necessary to distinguish θ from $\bar{\theta}$ (W^+ from W^-), semi-leptonic decay modes should be used for the discrimination. $\operatorname{Re}[\mathcal{M}_{\lambda_1\lambda_2}^{RR} \cdot (\mathcal{M}_{\lambda_1\lambda_2}^{LL})^*]$ and $\operatorname{Im}[\mathcal{M}_{\lambda_1\lambda_2}^{RR} \cdot (\mathcal{M}_{\lambda_1\lambda_2}^{LL})^*]$ are obtained simply by projecting out the $\cos(\phi - \bar{\phi})$ and $\sin(\phi - \bar{\phi})$ distributions. Both ϕ and $\bar{\phi}$ are observable when the W^+W^- pair decays semi-leptonically. Because the above four distributions can be measured independently, consistency among the four measurements can be checked.

We note here that the cross section for $\lambda_1 = \lambda_2 = \lambda$ without observing the W polariza-

tion can be written compactly as follows:

$$\begin{aligned}
\frac{d\hat{\sigma}_{\lambda\lambda}}{d\cos\Theta d\cos\theta d\cos\bar{\theta} d\phi d\bar{\phi}} &= \frac{3\beta}{32\pi\hat{s}} \times \frac{1}{16\pi^2} \times \\
&\{ |\mathcal{M}_{\lambda\lambda}^{RR}|^2 [(B_L^2 + B_T^2)(1 + \cos\theta \cos\bar{\theta}) + 2B_L B_T(1 - \cos\theta \cos\bar{\theta}) + (B_L^2 - B_T^2)(\cos\theta + \cos\bar{\theta})] \\
&+ |\mathcal{M}_{\lambda\lambda}^{LL}|^2 [(B_L^2 + B_T^2)(1 + \cos\theta \cos\bar{\theta}) + 2B_L B_T(1 - \cos\theta \cos\bar{\theta}) - (B_L^2 - B_T^2)(\cos\theta + \cos\bar{\theta})] \\
&+ 2\text{Re} [\mathcal{M}_{\lambda\lambda}^{RR}(\mathcal{M}_{\lambda\lambda}^{LL})^*] [(B_L - B_T)^2 \sin\theta \sin\bar{\theta} \cos(\phi - \bar{\phi})] \\
&+ 2\text{Im} [\mathcal{M}_{\lambda\lambda}^{RR}(\mathcal{M}_{\lambda\lambda}^{LL})^*] [-(B_L - B_T)^2 \sin\theta \sin\bar{\theta} \sin(\phi - \bar{\phi})] \}.
\end{aligned} \tag{3.14}$$

Because B_L and B_T have different numerical values, $B_L \simeq 0.7$ and $B_T \simeq 0.3$, we can obtain the four observables $|\mathcal{M}_{\lambda\lambda}^{RR}|^2$, $|\mathcal{M}_{\lambda\lambda}^{LL}|^2$, $\text{Re}[\mathcal{M}_{\lambda\lambda}^{RR}(\mathcal{M}_{\lambda\lambda}^{LL})^*]$ and $\text{Im}[\mathcal{M}_{\lambda\lambda}^{RR}(\mathcal{M}_{\lambda\lambda}^{LL})^*]$ even without observing the W polarization. In the following discussions, we adopt the simple expression eq. (3.14) in order to avoid repeating similar equations four times. It should be understood that the measurements can be improved significantly by using the W polarization information, as shown in eqs. (3.10) to (3.13).

4 Numerical Estimates

4.1 Convoluted cross sections with energy distribution of photon beams

The Compton back-scattered photons have broad energy distribution with the maximal value $E_\gamma^{max} = \frac{x}{x+1} E_e$ with $x \equiv 4E_e\omega_L/m_e^2$, in the zero angle limit of the Compton scattering. E_e and ω_L are the electron and laser photon energy. The circularly polarized laser photons and longitudinally polarized electrons help the broad distribution to peak near the high-energy end point where the colliding photons are highly polarized.

Fig. 1 shows the $\gamma\gamma$ collision energy distribution which is calculated by the tree-level formula of the backward Compton scattering [4] for $x = 4.8$ assuming complete polarization for laser photons ($P_l = -1.0$) and 90% polarization for electrons ($P_e = 0.9$). The distributions are shown for each combination of $\gamma\gamma$ helicities. The horizontal axis indicates the $\gamma\gamma$

collision energy ($\sqrt{\hat{s}}$) normalized by the ee c.o.m. energy (\sqrt{s}), that is, $z = \sqrt{\hat{s}}/\sqrt{s}$. The large z region where the energy distribution is peaked and dominated by the $++$ combination ($\lambda_1 = \lambda_2 = +$) is most useful for the study of $J_z = 0$ mode in the $\gamma\gamma$ collision. It is

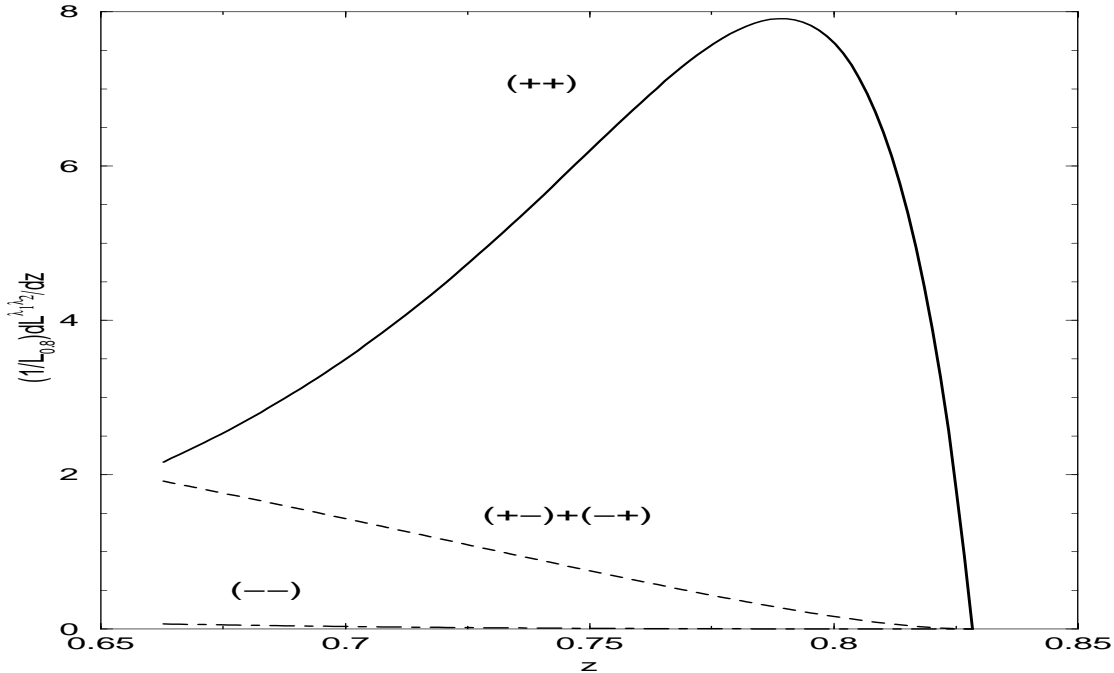


Figure 1: The $\gamma\gamma$ luminosity functions normalized by $\mathcal{L}_{0.8}$, the luminosity integrated over the region $z \geq 0.8z_m$ where $z = \sqrt{s}_{\gamma\gamma}/\sqrt{s}_{ee}$ and $z_m = x/(x+1)$ is the maximum energy fraction. The distributions of different $\gamma\gamma$ helicity combinations, $(++)$, $(--)$, $(+-)$ and $(-+)$, are shown separately for $P_l = -1.0$, $P_e = 0.9$ and $x = 4.8$.

expected that the $\gamma\gamma$ luminosity in the region $z \geq 0.8z_m = 0.8\frac{x}{x+1}$ will account for about 10% of the geometric luminosity of electron-electron collisions, L_{ee}^{geom} [4],

$$\mathcal{L}_{0.8} \equiv \sum_{\lambda_1, \lambda_2} \int_{0.8z_m}^{z_m} dz \frac{d\mathcal{L}^{\lambda_1 \lambda_2}}{dz} \approx 0.1 \mathcal{L}_{ee}^{geom}. \quad (4.1)$$

In the lower energy region, $z \lesssim 0.8z_m$, both the spectrum and the polarization receive significant non-linear corrections so that the Compton scattering becomes a poor approximation.

We therefore normalized the $\gamma\gamma$ luminosity distributions by $\mathcal{L}_{0.8}$ in Fig. 1. All our convoluted cross sections are calculated for the $\gamma\gamma$ luminosity distributions normalized by $\mathcal{L}_{0.8}$. The expected number of events is hence obtained by multiplying the convoluted cross sections by $\mathcal{L}_{0.8} \approx 0.1\mathcal{L}_{ee}^{geom}$. Though our luminosity functions based on Compton scattering are not reliable at $z \lesssim 0.8z_m$ or $z \lesssim 0.66$ for $x = 4.8$, in this report we consider $t\bar{t}$ production at a $\sqrt{s}_{ee} = 500$ GeV collider, and hence our study is limited to the region $z \geq 2m_t/\sqrt{s} \approx 0.7$.

Because of the above broad $\gamma\gamma$ energy distributions, we cannot observe the $\gamma\gamma \rightarrow t\bar{t}$ production cross section at a given $\gamma\gamma$ energy, $\sqrt{s}_{\gamma\gamma} \equiv \sqrt{\hat{s}}$. Instead we should use the invariant mass of the final $t\bar{t}$ pair system, $m_{t\bar{t}}$, as a measure of the colliding $\gamma\gamma$ energy. Although $m_{t\bar{t}}$ can in principle be measured event by event when a produced $t\bar{t}$ pair decays hadronically or semi-leptonically, we should expect uncertainties due to finite resolutions and non-Hermiticity of a detector. We introduce a smearing function

$$G(\sqrt{\hat{s}} - m_{t\bar{t}}, \Delta) = \frac{1}{\sqrt{2\pi}\Delta} \exp\left[-\frac{1}{2}\left(\frac{\sqrt{\hat{s}} - m_{t\bar{t}}}{\Delta}\right)^2\right], \quad (4.2)$$

between the true $m_{t\bar{t}} = \sqrt{\hat{s}}$ and the $m_{t\bar{t}}$. The observable cross sections can then be approximated as

$$\frac{d\sigma}{dm_{t\bar{t}}} \equiv \int_0^{z_m\sqrt{s}} d\sqrt{\hat{s}} \sum_{\lambda_1, \lambda_2} \frac{1}{\mathcal{L}_{0.8}} \frac{d\mathcal{L}^{\lambda_1\lambda_2}}{d\sqrt{\hat{s}}} \hat{\sigma}_{\lambda_1\lambda_2}(\sqrt{\hat{s}}) G(\sqrt{\hat{s}} - m_{t\bar{t}}, \Delta). \quad (4.3)$$

When we set $\Delta = 0$ GeV, the $m_{t\bar{t}}$ distributions reproduce the $\sqrt{s}_{\gamma\gamma}$ distributions.

In eq. (4.3), the $\gamma\gamma$ luminosity integrated over $z \geq 0.8z_m$ is denoted by $\mathcal{L}_{0.8}$ and the luminosity distribution for each $\gamma\gamma$ helicity combination is expressed by $d\mathcal{L}^{\lambda_1\lambda_2}/d\sqrt{\hat{s}}$. Thus, the expected number of events with $m_{min} \leq m_{t\bar{t}} \leq m_{max}$ is estimated by the formula;

$$N(m_{min} \leq m_{t\bar{t}} \leq m_{max}) = 0.1L_{ee}^{geom} \times \int_{m_{min}}^{m_{max}} dm_{t\bar{t}} \frac{d\sigma}{dm_{t\bar{t}}}. \quad (4.4)$$

It is notable that the geometric ee luminosity L_{ee}^{geom} can be larger than the nominal e^+e^- luminosity L_{ee} . According to the TESLA design [2],

$$L_{ee} = 3 \times 10^{34} \text{cm}^{-2}\text{s}^{-1}, \quad L_{ee}^{geom} = 12 \times 10^{34} \text{cm}^{-2}\text{s}^{-1} \quad (4.5)$$

at $\sqrt{s} = 500$ GeV have been reported.

4.2 Results

We consider the decay angular distribution of $t\bar{t}$ pairs produced via $\gamma\gamma$ collisions, and express the convoluted cross section in terms of four observables, Σ_1 to Σ_4 , which contain all the information about the $\gamma\gamma \rightarrow t\bar{t}$ helicity amplitudes. When we do not study W^+ and W^- decay angular distributions, the differential cross sections is expressed as

$$\begin{aligned}
& \frac{d\sigma}{dm_{t\bar{t}} d\cos\theta d\phi d\cos\bar{\theta} d\bar{\phi}} \\
&= \int d\sqrt{\hat{s}} \sum_{\lambda_1, \lambda_2} \left(\frac{1}{\mathcal{L}_{0.8}} \frac{d\mathcal{L}^{\lambda_1\lambda_2}}{d\sqrt{\hat{s}}} \right) \left(\frac{d\hat{\sigma}_{\lambda_1\lambda_2}(\sqrt{\hat{s}})}{d\cos\theta d\phi d\cos\bar{\theta} d\bar{\phi}} \right) G(\sqrt{\hat{s}} - m_{t\bar{t}}, \Delta) \\
&\equiv \{ \Sigma_1(m_{t\bar{t}}) [(B_L^2 + B_T^2)(1 + \cos\theta \cos\bar{\theta}) + 2B_L B_T(1 - \cos\theta \cos\bar{\theta}) + (B_L^2 - B_T^2)(\cos\theta + \cos\bar{\theta})] \\
&+ \Sigma_2(m_{t\bar{t}}) [(B_L^2 + B_T^2)(1 + \cos\theta \cos\bar{\theta}) + 2B_L B_T(1 - \cos\theta \cos\bar{\theta}) - (B_L^2 - B_T^2)(\cos\theta + \cos\bar{\theta})] \\
&+ \Sigma_3(m_{t\bar{t}}) [(B_L - B_T)^2 \sin\theta \sin\bar{\theta} \cos(\phi - \bar{\phi})] \\
&+ \Sigma_4(m_{t\bar{t}}) [-(B_L - B_T)^2 \sin\theta \sin\bar{\theta} \sin(\phi - \bar{\phi})] \} / 16\pi^2 \\
&+ [(\sigma = -\bar{\sigma}) \text{ contributions}].
\end{aligned} \tag{4.6}$$

Here small non-resonant contributions from $\sigma = -\bar{\sigma}$ (RL or LR) events are not shown explicitly. The four coefficients of the distinct decay angular distributions are

$$\begin{aligned}
\Sigma_i(m_{t\bar{t}}) = \int d\sqrt{\hat{s}} \sum_{\lambda_1, \lambda_2} \left(\frac{1}{\mathcal{L}_{0.8}} \frac{d\mathcal{L}^{\lambda_1\lambda_2}}{d\sqrt{\hat{s}}} \right) \left(\frac{3\beta}{32\pi\hat{s}} \int S_{\lambda_1\lambda_2}^i(\Theta, \sqrt{\hat{s}}) d\cos\Theta \right) G(\sqrt{\hat{s}} - m_{t\bar{t}}, \Delta), \tag{4.7} \\
\text{for } i = 1 - 4,
\end{aligned}$$

where the functions $S_{\lambda_1\lambda_2}^i$ contain all the information about the $\gamma\gamma \rightarrow t\bar{t}$ helicity amplitudes:

$$\begin{aligned}
S_{\lambda_1\lambda_2}^1 &= |\mathcal{M}_{\lambda_1\lambda_2}^{RR}|^2, \\
S_{\lambda_1\lambda_2}^2 &= |\mathcal{M}_{\lambda_1\lambda_2}^{LL}|^2, \\
S_{\lambda_1\lambda_2}^3 &= 2 \operatorname{Re} [\mathcal{M}_{\lambda_1\lambda_2}^{RR} (\mathcal{M}_{\lambda_1\lambda_2}^{LL})^*], \\
S_{\lambda_1\lambda_2}^4 &= 2 \operatorname{Im} [\mathcal{M}_{\lambda_1\lambda_2}^{RR} (\mathcal{M}_{\lambda_1\lambda_2}^{LL})^*].
\end{aligned} \tag{4.8}$$

A few remarks about eq. (4.6) are in order. The compact expression for the differential cross section in terms of the observable $m_{t\bar{t}}$, the $t \rightarrow bW^+$ decay angles θ and ϕ , and the

$\bar{t} \rightarrow \bar{b}W^-$ decay angles $\bar{\theta}$ and $\bar{\phi}$ are obtained by integrating out the $\gamma\gamma \rightarrow t\bar{t}$ scattering angle Θ , the W^+ decay angles θ^* and ϕ^* , and the W^- decay angles $\bar{\theta}^*$ and $\bar{\phi}^*$; see eq. (3.8). We do not lose much information by the integration over $\cos \Theta$ because the resonant $J = 0$ amplitudes do not depend on $\cos \Theta$ and because the $\cos \Theta$ dependences of the interfering QED amplitudes are mild near the $t\bar{t}$ threshold; $\beta = 0.48$ at $\sqrt{s}_{\gamma\gamma} = 400$ GeV. As explained in Sec. 3.2, a careful study of W^+ and W^- decay angular distributions should give us independent measurements of the observables Σ_1 to Σ_4 , and should therefore reduce errors.

The four observables Σ_1 to Σ_4 of eq. (4.6) are shown in Fig. 2 for $\Delta = 0$ GeV (no smearing by detector resolution), Fig. 3 for $\Delta = 3$ GeV and in Fig. 4 for $\Delta = 6$ GeV. The predictions of the A and H productions are shown by thick-solid and thick-dashed curves, respectively. The QED predictions are shown by the thin-solid lines. The quantity $\Sigma_1 + \Sigma_2$ is simply the total $t\bar{t}$ production cross section, smeared by the resolution factor of Δ . We show Σ_2 instead of Σ_1 because the A and H production amplitudes interfere with the QED amplitudes differently in the $\lambda_1 = \lambda_2 = +$ to $\sigma = \bar{\sigma} = L$ amplitudes.

When we draw the predictions of A and H productions in Figs. 2, 3 and 4, we adopt a MSSM prediction for the A production, while the H production curves are drawn by using the amplitudes \mathcal{M}_H which are obtained from the \mathcal{M}_A for the same mass and width and the same magnitudes for the partial widths to $\gamma\gamma$ and $t\bar{t}$. The MSSM parameters used for calculating \mathcal{M}_A are as follows: $m_A = 400$ GeV, $\tan \beta = 3$, $m_{\tilde{f}} = 1$ TeV, $M_2 = 500$ GeV, $\mu = -500$ GeV. We find $m_A = 400$ GeV, $\Gamma_A = 1.75$ GeV, $\text{Br}(A \rightarrow \gamma\gamma) = 1.53 \times 10^{-5}$ and $\text{Br}(A \rightarrow t\bar{t}) = 0.946$ for the above parameters [18]. The H production amplitudes \mathcal{M}_H are thus obtained from \mathcal{M}_A by keeping the mass, width and partial widths common in order to show clearly the sensitivity of the four observables to the CP property of the produced spinless boson. For the collider parameters, we use $E_e = 250$ GeV, $P_l = -1.0$, $P_e = 0.9$ and $x = 4.8$, where colliding photons are highly polarized to be $+$ around $\sqrt{s} = 400$ GeV; see Fig. 1. Since the effects from the $(\lambda_1\lambda_2) = (+-)$, $(-+)$ and $(--)$ combinations on the observables are less than 1% around the peak region, they are neglected here. In this limit,

the quantities S_{1-4} in eq. (4.8) can be expressed by \mathcal{M}_t and \mathcal{M}_ϕ as

$$S_{++}^1 = |\mathcal{M}_t|^2 + |\mathcal{M}_\phi|^2 + 2\mathcal{M}_t \operatorname{Re}[\mathcal{M}_\phi], \quad (4.9)$$

$$S_{++}^2 = \left(\frac{1-\beta}{1+\beta}\right)^2 |\mathcal{M}_t|^2 + |\mathcal{M}_\phi|^2 \pm 2\frac{1-\beta}{1+\beta}\mathcal{M}_t \operatorname{Re}[\mathcal{M}_\phi], \quad (4.10)$$

$$S_{++}^3 = 2\frac{1-\beta}{1+\beta} |\mathcal{M}_t|^2 \pm 2|\mathcal{M}_\phi|^2 + 2\left(\frac{1-\beta}{1+\beta} \pm 1\right) \mathcal{M}_t \operatorname{Re}[\mathcal{M}_\phi], \quad (4.11)$$

$$S_{++}^4 = 2\left(\frac{1-\beta}{1+\beta} \mp 1\right) \mathcal{M}_t \operatorname{Im}[\mathcal{M}_\phi], \quad (4.12)$$

where the upper and lower signs are adopted for A and H , respectively.

Let us now examine carefully the results shown in Fig. 2 to 4. For the total production cross section $\Sigma_1 + \Sigma_2$, it can be clearly observed in Fig. 2 that the A production amplitudes receive stronger constructive (destructive) interference below (above) the resonance peak than the H production amplitudes. A sharp dip above the resonance peak for the A production line-shape may be considered as a signal of a CP-odd resonance production. However, the difference between the A and H line shapes diminishes by smearing. A hint of strong destructive interference survives in Fig. 3 for the smearing with $\Delta = 3$ GeV, but the difference essentially disappears in Fig. 4 for $\Delta = 6$ GeV. The two thick curves for $\Sigma_1 + \Sigma_2$ in Fig. 4 can only tell broad enhancement over the QED prediction, which may be fitted well by both A and H production assumptions with slightly different mass and width values.

The Σ_2 shows not only large contribution of the Higgs production but also the interference effects which have opposite contribution for the A and H production. The magnitudes of the effects are small because the QED amplitude which interferes with the Higgs production amplitudes is suppressed by the factor of $\frac{1-\beta}{1+\beta}$; see Table 2. Here the distinctive signature of the negative interference below the resonance for the H production may survive even for the resolution of $\Delta = 6$ GeV in Fig. 4.

The interference effects we observe in the Σ_3 is larger for A than for H due to the factor of $\frac{1-\beta}{1+\beta} \pm 1$ in eq. (4.11). A sharp dip for the A production line-shape and a small

excess for the H production line-shape above the resonance peaks are the effects. The destructive interference effect for A may survive even in Fig. 4 for $\Delta = 6$ GeV, whereas the small constructive interference effect for H almost disappears in Fig. 4. It is notable that the effects of the Higgs production has opposite signs for A and H in eq. (4.11). This oppositeness causes that the A production enhances Σ_3 above the QED prediction near the peak of the total cross section $\Sigma_1 + \Sigma_2$, whereas the H production predicts smaller Σ_3 than the QED prediction around the peak of the cross section. This feature seems to persist even with faint $t\bar{t}$ mass resolution, in Fig. 3 for $\Delta = 3$ GeV and Fig. 4 for $\Delta = 6$ GeV.

As for the Σ_4 , the pure interference effects can be observed. The QED amplitudes predict $\Sigma_4=0$ because we adopt the tree-level amplitudes in our analysis². The A production predicts negative and the H production predicts positive effects for Σ_4 around the production peak. The difference in the magnitudes comes from the factor of $\frac{1-\beta}{1+\beta} \mp 1$ in eq. (4.12). These characteristics appear even considering the detector resolution as is shown in Fig. 3 for $\Delta = 3$ GeV and Fig. 4 for $\Delta = 6$ GeV. The imaginary part of the interference term, Σ_4 , discriminates between A and H most clearly.

Summing up, we have made the following observation in this subsection. The $m_{t\bar{t}}$ dependence of the total production cross section, $\Sigma_1 + \Sigma_2$, can in principle reveal the difference between A and H productions, as shown in Fig. 2. However the distinctive signatures of the A productions, the constructive interference below the resonance and the pronounced destructive interference above the resonance diminish as the $m_{t\bar{t}}$ measurement resolution becomes worse to $\Delta = 3$ GeV (Fig. 3) and to $\Delta = 6$ GeV (Fig. 4). It is only the tiny destructive interference effects above the resonance in Fig. 4 which signals the production of A rather than H . The situation slightly improves by observing the Σ_2 component by selecting those events where the produced top-quarks are both left-handed. Here the distinctive signature of the negative interference below the resonance for the H

²The continuum $\gamma\gamma \rightarrow t\bar{t}$ amplitudes should have imaginary parts of the order of α_s in QCD perturbation theory.

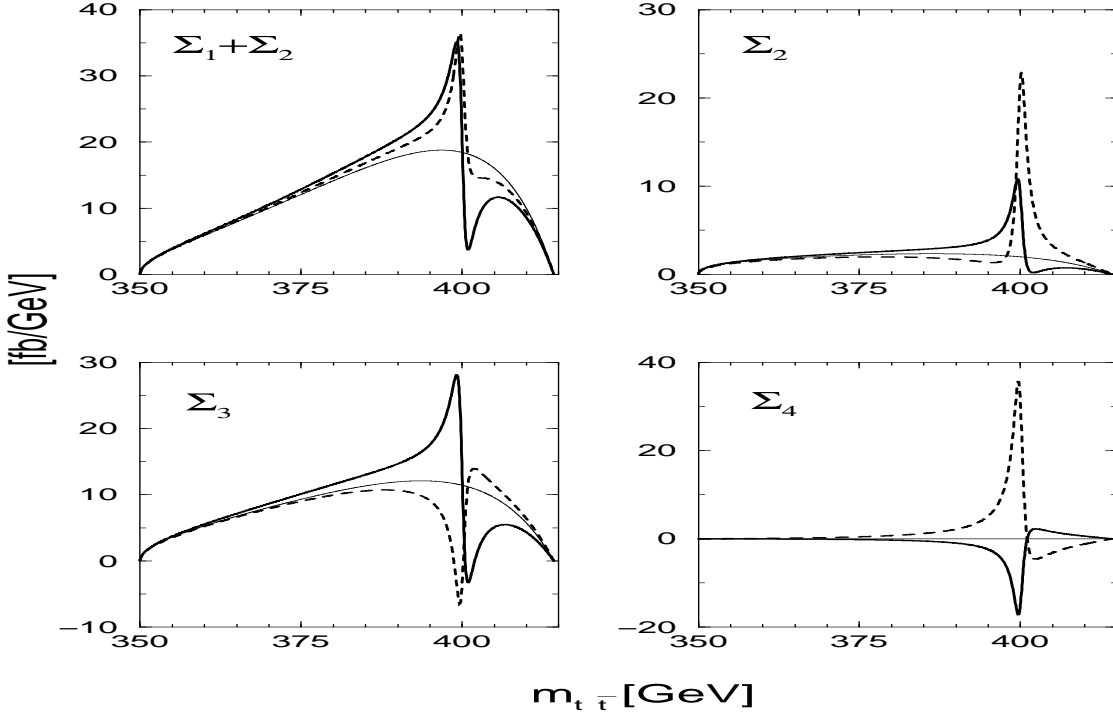


Figure 2: The observables Σ_1 to Σ_4 with no smearing by detector resolution. The thick solid (dashed) curves show the predictions for the A (H) production. The thin solid curves show the QED predictions with no Higgs production.

production may survive even for the resolution of $\Delta = 6$ GeV in Fig. 4. The cross section for $t_L\bar{t}_L$ production, however, is rather small as compared to the dominant $t_R\bar{t}_R$ production, because of the $(1 - \beta)/(1 + \beta)$ suppression factor in the corresponding QED amplitude; see Table 2. Further information are obtained by studying the interference between the $t_R\bar{t}_R$ and the $t_L\bar{t}_L$ amplitudes in the observables Σ_3 and Σ_4 . The real part of the interference term, Σ_3 , shows that the A production enhances Σ_3 above the QED prediction near the peak of the total cross section, $\Sigma_1 + \Sigma_2$, whereas the H production predicts smaller Σ_3 than the QED prediction around the peak of the cross section. This feature seems to persist even with faint $t\bar{t}$ mass resolution, in Fig. 3 for $\Delta = 3$ GeV and Fig. 4 for $\Delta = 6$ GeV. Finally the

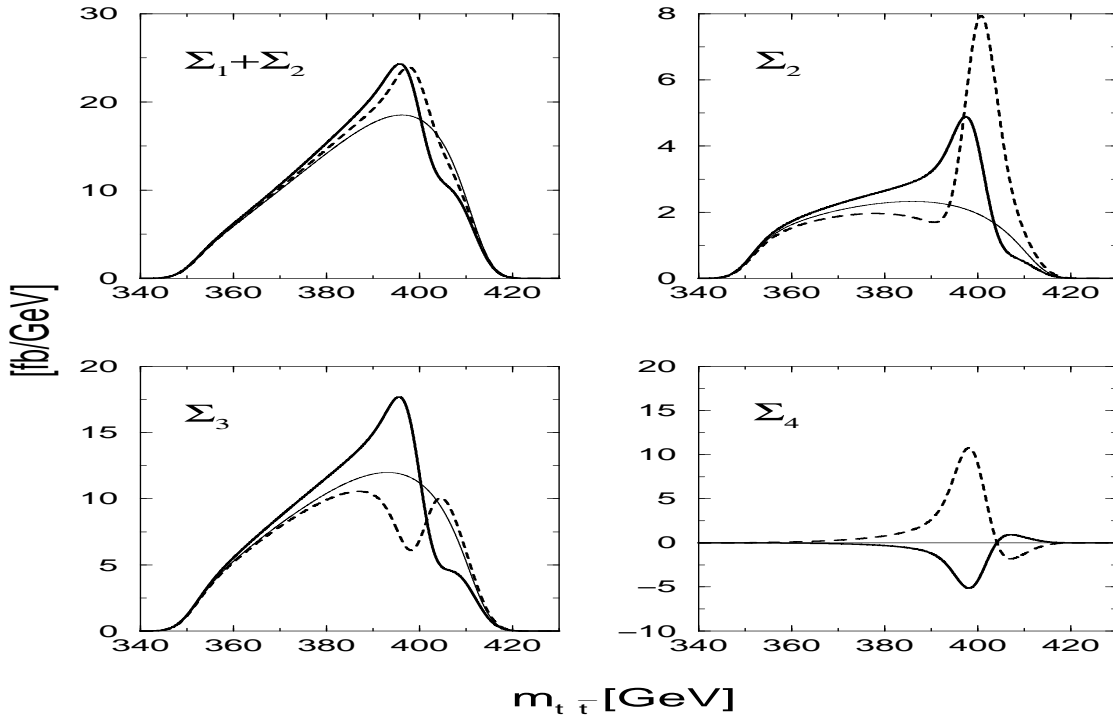


Figure 3: The observables Σ_1 to Σ_4 with the $t\bar{t}$ invariant mass measurement resolution factor $\Delta = 3$ GeV. The thick solid (dashed) curves show the predictions for the A (H) production. The thin solid curves show the QED predictions with no Higgs production.

imaginary part of the interference term, Σ_4 , discriminates between A and H most clearly. The A production predicts negative and the H production predicts positive effects for Σ_4 around the production peak. We therefore propose to use the four observables Σ_1 to Σ_4 in determining the CP property of the spin zero resonance in the $\gamma\gamma \rightarrow t\bar{t}$ channel.

In the above discussion, we studied four observables separately. Once they are derived individually, we can obtain their arbitrary linear combinations. The most powerful combinations for probing the CP parity of Higgs bosons are $\Sigma_1 + \Sigma_2 + \Sigma_3$ and $\Sigma_1 + \Sigma_2 - \Sigma_3$. The former combination receives contribution only from the CP-odd resonance, while the latter only from the CP-even resonance when CP is conserved. It is therefore straightforward to

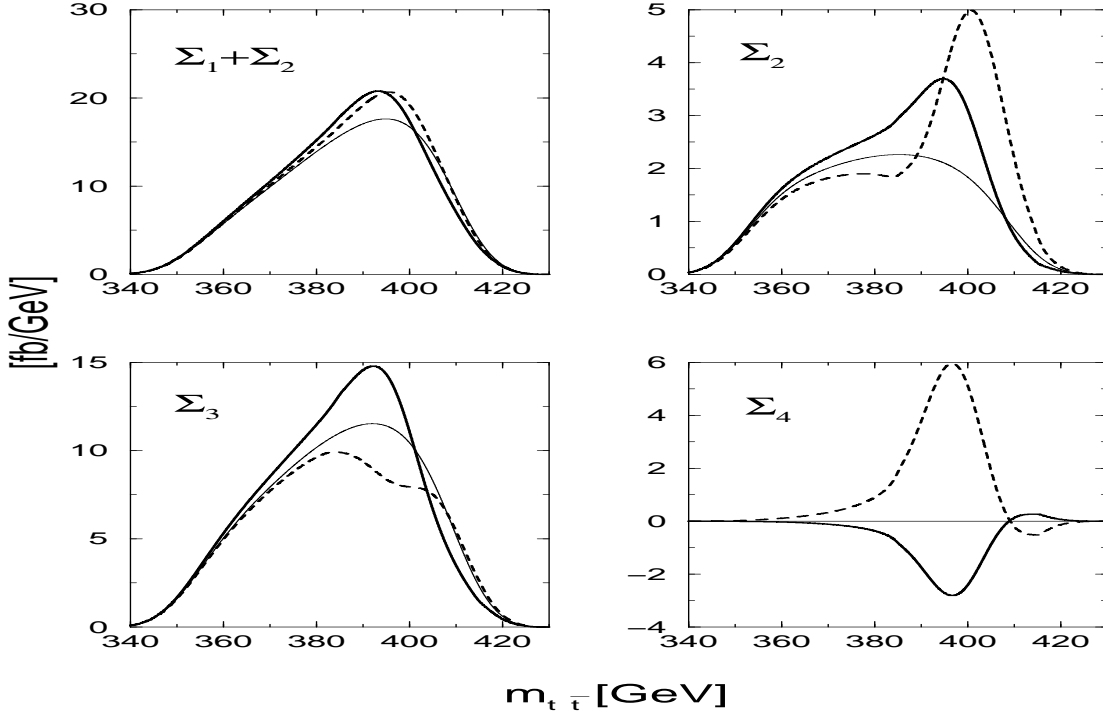


Figure 4: The observables Σ_1 to Σ_4 with the $t\bar{t}$ invariant mass measurement resolution factor $\Delta = 6$ GeV. The thick solid (dashed) curves show the predictions for the A (H) production. The thin solid curves show the QED predictions with no Higgs production.

separate the CP-even and CP-odd resonances, even when their masses are degenerate.

4.3 Effects of the $\gamma\gamma\phi$ phase on the observables

In this subsection, we study the $\arg(b_\gamma^\phi)$ dependence of the four observables studied in the previous subsection. We first re-parameterize the $J_z = 0$ amplitudes of eq. (2.2) as follows:

$$\mathcal{M}_{\lambda\lambda}^{\sigma\sigma} = [\mathcal{M}_t]_{\lambda\lambda}^{\sigma\sigma} + \left(\frac{\sqrt{\hat{s}}}{m_\phi}\right)^3 r_\phi \cdot i \left[1 + \exp\left(2i \tan^{-1} \frac{s^2 - m_\phi^2}{m_\phi \Gamma_\phi}\right) \right], \quad (4.13)$$

where $r_H = \sigma\beta b_\gamma^H d_t^H m_H / (2\Gamma_H)$ and $r_A = \lambda b_\gamma^A d_t^A m_A / (2\Gamma_A)$. In this expression, the phase of the Breit-Wigner resonance amplitude is shifted by the phase of the r_ϕ factor which is essentially the phase of the $\gamma\gamma\phi$ vertex factor b_γ^ϕ if we neglect the phase in the $t\bar{t}\phi$ vertex

d_t^ϕ . It should also be noted that

$$|r_\phi|^2 = \frac{32\pi^2}{3\beta} \text{Br}(\phi \rightarrow \gamma\gamma) \text{Br}(\phi \rightarrow t\bar{t}). \quad (4.14)$$

In the above discussions, we draw the H production curves by assuming not only $m_H = m_A$, $\Gamma_H = \Gamma_A$ and $\text{Br}(H \rightarrow \gamma\gamma)\text{Br}(H \rightarrow t\bar{t}) = \text{Br}(A \rightarrow \gamma\gamma)\text{Br}(A \rightarrow t\bar{t})$, but also that the $\gamma\gamma \rightarrow H$ amplitude is proportional to the $\gamma\gamma \rightarrow A$ amplitude as a complex numbers,

$$b_\gamma^H = b_\gamma^A \left[\frac{\Gamma(H \rightarrow \gamma\gamma)}{\Gamma(A \rightarrow \gamma\gamma)} \right]^{1/2}. \quad (4.15)$$

We note here that the phase of the $H \rightarrow \gamma\gamma$ amplitude, $\arg(b_\gamma^H)$, and that of the $A \rightarrow \gamma\gamma$ amplitude, $\arg(b_\gamma^A)$, depend significantly in the model parameters. As an example, we show in Table 3 the MSSM prediction for the real and imaginary parts of b_γ^A and b_γ^H . Here, we calculate the A and H masses and couplings for the MSSM parameters; $m_A = 400$ GeV, $\tan\beta = 3$, $m_{\tilde{f}} = 1$ TeV, $M_2 = 500$ GeV, $\mu = -500$ GeV. We find that $\arg(b_\gamma^A)$ is much larger than $\arg(b_\gamma^H)$. The large imaginary part of b_γ^A is a result of the s -wave $A \rightarrow t\bar{t}$ decay near the $t\bar{t}$ production threshold. The imaginary part of b_γ^H is suppressed by the p -wave $H \rightarrow t\bar{t}$ decay and also by the partial cancellation due to the $H \rightarrow W^+W^-$ contribution. Therefore, in the framework of the two Higgs doublet model without any new particles which contribute to the vertex significantly, the A boson has relatively large phase and the H boson has tiny phase. Because the imaginary part of the $\phi \rightarrow \gamma\gamma$ amplitude is a sum of the contribution from the ϕ decay modes into charged particles whereas the real part receives contribution from all the charged particles, we expect that $\arg(b_\gamma^\phi)$ is a good probe of heavy charged particles.

Fig. 5 shows plots of the amplitudes $\mathcal{M}_{\lambda\lambda}^{\sigma\sigma}$ on the complex plane where the scattering angle Θ is fixed to be zero as a sample. The amplitudes with the A (H) production is in the left (right) side. Since the tree amplitudes $[\mathcal{M}_t]_{\lambda\lambda}^{\sigma\sigma}$ are real and almost constant around the resonance, the plots draw a counterclockwise circle which have the beginning- and end-points on the real axis as \hat{s} increases. The circles which have the beginning points nearer

(further) from the origin correspond to $\mathcal{M}_{\lambda\lambda}^{-\lambda,-\lambda}$ ($\mathcal{M}_{\lambda\lambda}^{\lambda\lambda}$). Two cases of $\arg(b_\gamma^\phi)$ are considered. One is the case where b_γ^ϕ has no phase (solid curves), the other is $\arg(b_\gamma^\phi) = \pi/4$ (dashed curves). The solid and open small circles on the trajectories indicate the $\hat{s} = m_\phi^2$ points. When $m_\phi^2 - \hat{s} \gg m_\phi\Gamma_\phi$, the amplitudes are real positive numbers that are determined by the QED amplitudes of Table 1. As \hat{s} grows, the amplitudes make counterclockwise trajectories, and the magnitude of the resonance amplitude hits its maximum at $\hat{s} = m_\phi^2$. At $m_\phi^2 - \hat{s} \ll m_\phi\Gamma_\phi$, the amplitudes reduce to the real and positive QED amplitude again. The trajectories do not close because of the mild \hat{s} -dependence of the QED amplitudes.

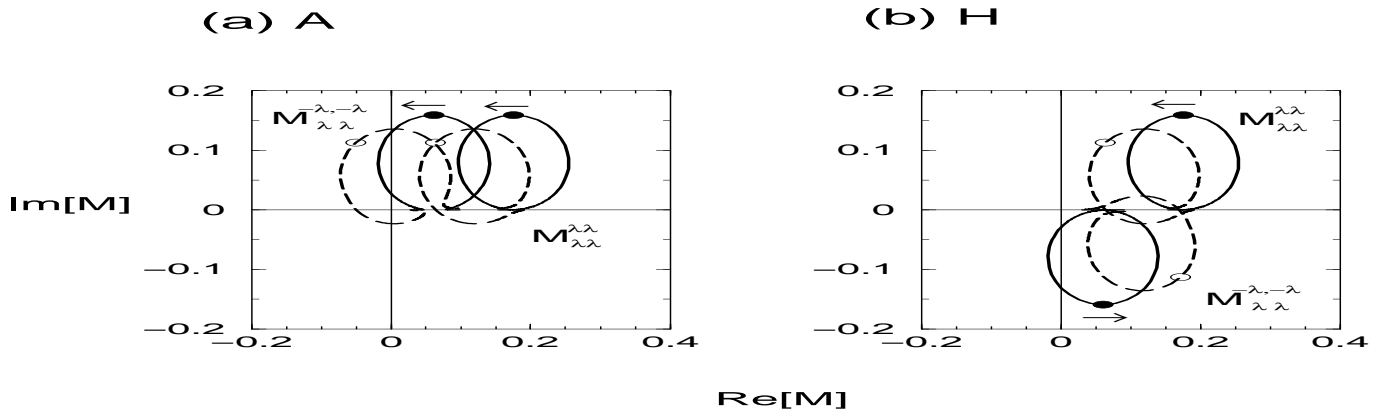


Figure 5: The \hat{s} -dependence of the $\gamma\gamma \rightarrow t\bar{t}$ amplitudes $\mathcal{M}_{\lambda\lambda}^{\sigma\sigma}$ at $\Theta = 0^\circ$. The amplitudes with A production are shown in the left figure, whereas those for H production are shown in the right. The cases of $\arg(b_\gamma^\phi) = 0$ and $\pi/4$ are denoted by the solid and dashed circles, respectively. The small arrows indicate the direction of increasing \hat{s} and the solid and open small circles on the trajectories show the $\hat{s} = m_\phi^2$ points. As \hat{s} grows the amplitudes make counterclockwise trajectories, and the magnitude of the resonance amplitude hits its maximum at $\hat{s} = m_\phi^2$.

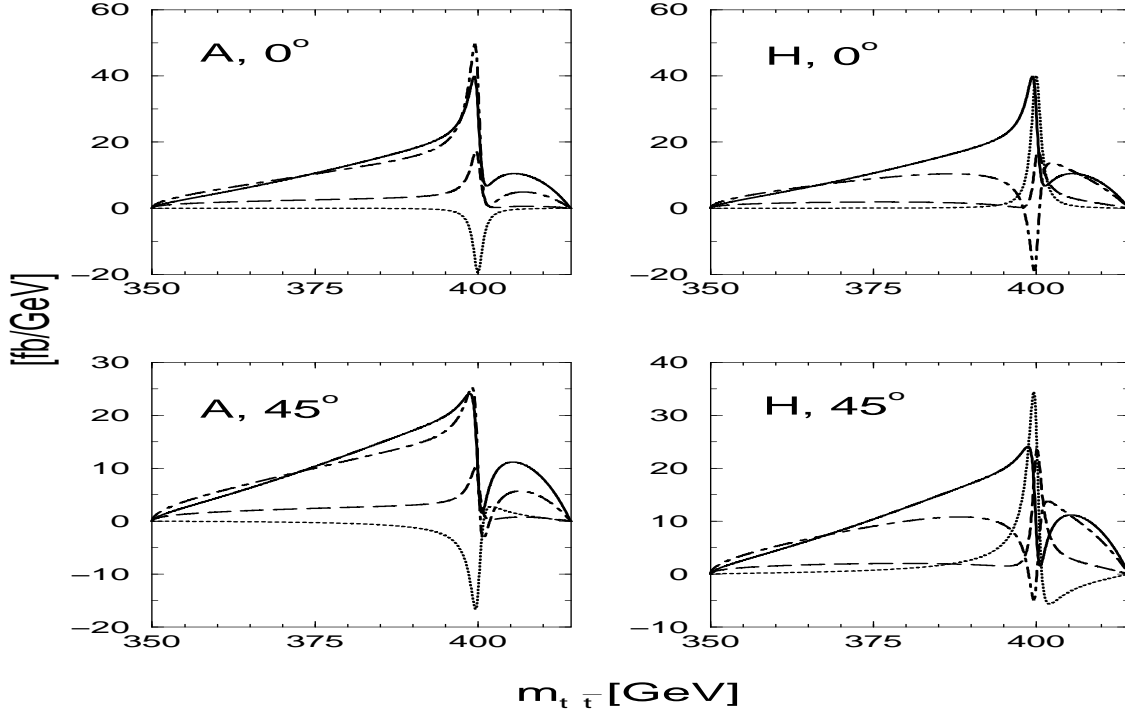


Figure 6: The observables Σ_1 to Σ_4 with no smearing by detector resolution. The solid, dashed, dot-dashed and dotted curves are Σ_1 , Σ_2 , Σ_3 and Σ_4 , respectively. The observables with A production are in the left (right) figures whereas those with the H production are shown in the right. The upper and lower figures show the case of $\arg(r_\phi) = 0$ and $\pi/4$, respectively.

The magnitudes of $\mathcal{M}_{\lambda\lambda}^{\sigma\sigma}$ have peaks at the furthest points from the origin on the trajectories. The $\sqrt{\hat{s}}$ values at which the amplitudes have the largest magnitude are almost similar between $\mathcal{M}_{\lambda\lambda}^{\lambda\lambda}$ and $\mathcal{M}_{\lambda\lambda}^{-\lambda,-\lambda}$ for the A production (slightly below the $\hat{s} = m_A^2$ point), while they are significantly different for the H production because the sign of the imaginary parts are opposite between $\mathcal{M}_{\lambda\lambda}^{-\lambda,-\lambda}$ and $\mathcal{M}_{\lambda\lambda}^{\lambda\lambda}$. The amplitude of $\mathcal{M}_{\lambda\lambda}^{\lambda\lambda}$ becomes maximum slightly below the $\hat{s} = m_H^2$ point, but that of $\mathcal{M}_{\lambda\lambda}^{-\lambda,-\lambda}$ hits the maximum at $\hat{s} > m_H^2$.

When we compare the $\arg(b_\gamma^A) = 0$ amplitudes (solid circles) and the $\arg(b_\gamma^A) = \pi/4$ amplitudes (dashed circles), we notice that the magnitudes of all the amplitudes are reduced

for $\arg(b_\gamma^A) > 0$ because the imaginary parts of the resonant amplitudes are positive for $\arg(b_\gamma^A) = 0$. It is notable that at $\hat{s} = m_A^2$ (solid and open circles along the trajectories), the real part of the $\mathcal{M}_{\lambda\lambda}^{-\lambda, -\lambda}$ amplitudes become negative when $\arg(b_\gamma^A) = \pi/4$. In case of the $\phi = H$ amplitudes shown in Fig. 5(b), the most notable feature is that the magnitude of the $\mathcal{M}_{\lambda\lambda}^{-\lambda, -\lambda}$ amplitudes increases for $\arg(b_\gamma^A) > 0$ because the sign of the imaginary part of the H resonant amplitude is negative for these amplitudes. On the other hand, the magnitudes of the $\mathcal{M}_{\lambda\lambda}^{\lambda\lambda}$ amplitudes decreases for $\arg(b_\gamma^A) > 0$ as in the case for the A production amplitudes.

We show in Fig. 6 the four observables Σ_1 to Σ_4 for the A production in the left, and for the H production in the right-hand side. The predictions for $\arg(b_\gamma^\phi) = 0$ are shown in the top figures, whereas those for $\arg(b_\gamma^\phi) = \pi/4$ are shown in the bottom figures.

We find that the features which are sensitive to the CP parity of the spinless boson ϕ , such as the interference pattern of Σ_3 and Σ_4 near the resonances, remain stable against varieties of $\arg(b_\gamma^\phi)$ between 0 and $\pi/4$. On the other hand the $\arg(b_\gamma^\phi)$ dependence of the four observables are significant enough that the phase of the $\gamma\gamma\phi$ vertex function may be measured experimentally by a careful study of all the observables.

Table 3: The values of b_γ^A and b_γ^H . The loops of t , b , W , $\tilde{\chi}_1^-$ and $\tilde{\chi}_2^-$ give large contribution to b_γ^H and b_γ^A under our parameterization; $m_A = 400$ GeV, $\tan\beta = 3$, $M_2 = 500$ GeV, $\mu = -500$ GeV and $M_{\tilde{f}} = 1$ TeV. $m_H = 403.8$ GeV for the above parameters.

	$b_\gamma^A \times 10^4$	$b_\gamma^H \times 10^4$
total	$14 + 12i$	$11 + 1.3i$
t	$15 + 12i$	$12 + 3.3i$
b	$-0.19 + 0.15i$	$0.18 - 0.15i$
W	0.0	$-1.0 - 1.7i$
$\tilde{\chi}_1^-$	-1.1	-1.2
$\tilde{\chi}_2^-$	0.51	1.0

5 Conclusions

We have studied the effects of heavy Higgs bosons in $t\bar{t}$ production process at a PLC. We have introduced observables which include new type of interference by considering the angular correlation of decay products of top quarks, and found that they are useful for probing the CP nature of the produced Higgs boson. It has also been shown that variation in the complex phase of the $\gamma\gamma\phi$ vertex modify the magnitudes of the observables and the $\sqrt{\hat{s}}$ values where the observables have peaks and bottoms.

Further studies on the cases where the Higgs sector has CP non-conservation and/or a degenerate pair of heavy neutral bosons will be reported elsewhere [14]. The present study may motivate a careful study of the experimental resolution of the $t\bar{t}$ invariant mass measurements as well as a quantitative study on the accuracy of the resonance parameters, m_ϕ , Γ_ϕ , $\text{Br}(\phi \rightarrow \gamma\gamma)\text{Br}(\phi \rightarrow t\bar{t})$, $\arg(b_\gamma^\phi d_t^\phi)$, and its CP parity.

Acknowledgments The authors would like to thank T. Takahashi and I. Watanabe for useful comments. The work of EA is supported in part by the Grant-in-Aid for Scientific Research from MEXT, Japan.

A Amplitude for the process $\gamma\gamma \rightarrow t\bar{t} \rightarrow bf_1\bar{f}_2 \bar{b}f_3\bar{f}_4$

We describe the helicity amplitudes for the process $\gamma\gamma \rightarrow t\bar{t} \rightarrow bf_1\bar{f}_2 \bar{b}f_3\bar{f}_4$ as

$$\begin{aligned} \mathbf{M}_{\lambda_1\lambda_2}(\Theta; \theta, \phi, \bar{\theta}, \bar{\phi}; \theta^*, \phi^*, \bar{\theta}^*, \bar{\phi}^*) & \quad (\text{A.1}) \\ &= \sum_{\sigma=L,R} \sum_{\Lambda=-,0} \sum_{\bar{\Lambda}=0,+} \mathcal{M}_{\lambda_1\lambda_2}^{\sigma\bar{\sigma}}(\Theta) D_{\sigma}^{\Lambda}(\theta, \phi) \bar{D}_{\bar{\sigma}}^{\bar{\Lambda}}(\bar{\theta}, \bar{\phi}) W_{\Lambda}(\theta^*, \phi^*) \bar{W}_{\bar{\Lambda}}(\bar{\theta}^*, \bar{\phi}^*), \end{aligned}$$

in the zero-width limit of the top-quark and the W bosons. Here λ_1, λ_2 are the helicities of the colliding photons, $\mathcal{M}_{\lambda_1\lambda_2}^{\sigma\bar{\sigma}}(\Theta)$ is the $\gamma(\lambda_1)\gamma(\lambda_2) \rightarrow t(\sigma)\bar{t}(\bar{\sigma})$ scattering amplitudes at the scattering angle Θ in the $\gamma\gamma$ collision c.o.m. frame, D_{σ}^{Λ} and $\bar{D}_{\bar{\sigma}}^{\bar{\Lambda}}$ are the decay amplitudes for the processes $t_{\sigma} \rightarrow bW_{\Lambda}^{+}$ and $\bar{t}_{\bar{\sigma}} \rightarrow \bar{b}W_{\bar{\Lambda}}^{-}$ in the t and \bar{t} rest frame, respectively. W_{Λ} and $\bar{W}_{\bar{\Lambda}}$ are the decay amplitudes for the processes $W_{\Lambda}^{+} \rightarrow f_1\bar{f}_2$ and $W_{\bar{\Lambda}}^{-} \rightarrow f_3\bar{f}_4$ in the decaying W rest frames, in the massless fermion limit ($m_{f_i} = 0$). The decay amplitudes have the following simple forms in the phase connection of Ref. [12, 19]:

$$\begin{aligned} D_L^0 &= \sqrt{\frac{B_L}{2\pi}} \sin \frac{\theta}{2}, & D_L^- &= \sqrt{\frac{B_T}{2\pi}} \cos \frac{\theta}{2}, & D_R^0 &= \sqrt{\frac{B_L}{2\pi}} \cos \frac{\theta}{2} e^{i\phi}, & D_R^- &= -\sqrt{\frac{B_T}{2\pi}} \sin \frac{\theta}{2} e^{i\phi}, \\ \bar{D}_L^0 &= -\sqrt{\frac{B_L}{2\pi}} \sin \frac{\bar{\theta}}{2}, & \bar{D}_L^+ &= \sqrt{\frac{B_T}{2\pi}} \cos \frac{\bar{\theta}}{2}, & \bar{D}_R^0 &= -\sqrt{\frac{B_L}{2\pi}} \cos \frac{\bar{\theta}}{2} e^{-i\bar{\phi}}, & \bar{D}_R^+ &= -\sqrt{\frac{B_T}{2\pi}} \sin \frac{\bar{\theta}}{2} e^{-i\bar{\phi}}, \end{aligned} \quad (\text{A.2})$$

and

$$\begin{aligned} W_0 &= \sqrt{\frac{3}{8\pi} B_{12}} \sin \theta^*, & W_- &= \sqrt{\frac{3}{8\pi} B_{12}} \frac{1-\cos \theta^*}{\sqrt{2}} e^{-i\phi^*}, \\ \bar{W}_0 &= \sqrt{\frac{3}{8\pi} B_{34}} \sin \bar{\theta}^*, & \bar{W}_+ &= -\sqrt{\frac{3}{8\pi} B_{34}} \frac{1-\cos \bar{\theta}^*}{\sqrt{2}} e^{i\bar{\phi}^*}. \end{aligned}$$

Here the decay amplitudes are normalized as

$$\begin{aligned} \int |D_{\sigma}^{-}|^2 d \cos \theta d\phi &= \int |\bar{D}_{\bar{\sigma}}^{+}|^2 d \cos \bar{\theta} d\bar{\phi} = B_T = \frac{2m_W^2}{m_t^2 + 2m_W^2}, & (\text{A.3}) \\ \int |D_{\sigma}^0|^2 d \cos \theta d\phi &= \int |\bar{D}_{\bar{\sigma}}^0|^2 d \cos \bar{\theta} d\bar{\phi} = B_L = \frac{m_t^2}{m_t^2 + 2m_W^2}, \end{aligned}$$

and

$$\begin{aligned} \int |W_{\Lambda}|^2 d \cos \theta^* d\phi^* &= B_{12}, & (\text{A.4}) \\ \int |\bar{W}_{\bar{\Lambda}}|^2 d \cos \bar{\theta}^* d\bar{\phi}^* &= B_{34}, \end{aligned}$$

where B_{12} is the branching fraction of $W^+ \rightarrow f_1 \bar{f}_2$ decays, and B_{34} is that of $W^- \rightarrow f_3 \bar{f}_4$. The angles θ and ϕ ($\bar{\theta}$ and $\bar{\phi}$) are, respectively, the polar and azimuthal angles of W^+ (W^-) in the t (\bar{t}) rest frame where the common polar axis is chosen along the t -momentum direction in the $\gamma\gamma$ collision c.m. frame, and the azimuthal angles ϕ and $\bar{\phi}$ are measured from the $\gamma\gamma \rightarrow t\bar{t}$ scattering plane. θ^* and ϕ^* are, respectively, the polar and azimuthal angles of \bar{f}_2 in the $W^+ \rightarrow f_1 \bar{f}_2$ decay rest frame, whereas $\bar{\theta}^*$ and $\bar{\phi}^*$ are those of f_3 in the $W^- \rightarrow f_3 \bar{f}_4$ rest frame. We choose the \bar{f}_2 and f_3 momenta in the above decays so that the angles are those of the charged leptons in the decays $W^+ \rightarrow \nu_l l^+$ and $W^- \rightarrow l^- \bar{\nu}_l$. The polar axis are chosen along the W^\pm momentum in the parent t or \bar{t} rest frame, while the azimuthal angles ϕ^* and $\bar{\phi}^*$ are measured from the $t \rightarrow bW^+$ and $\bar{t} \rightarrow \bar{b}W^-$ decay planes, respectively, in the $\gamma\gamma$ collision c.m. frame.

The amplitudes (A.1) can now be expressed solely in terms of the $\gamma\gamma \rightarrow t\bar{t}$ amplitudes $\mathcal{M}_{\lambda_1 \lambda_2}^{\sigma \bar{\sigma}}(\Theta)$:

$$\begin{aligned}
& \mathbf{M}_{\lambda_1 \lambda_2}(\Theta; \theta, \phi, \bar{\theta}, \bar{\phi}; \theta^*, \phi^*, \bar{\theta}^*, \bar{\phi}^*) / \left(\frac{3}{16\pi^2} \sqrt{B_{12} B_{34}} \right) \quad (\text{A.5}) \\
= & \mathcal{M}_{\lambda_1 \lambda_2}^{LL}(\Theta) \left\{ -B_L \sin \frac{\theta}{2} \sin \frac{\bar{\theta}}{2} \sin \theta^* \sin \bar{\theta}^* \right. \\
& - \sqrt{B_L B_T} \cos \frac{\theta}{2} \sin \frac{\bar{\theta}}{2} \frac{1 - \cos \theta^*}{\sqrt{2}} \sin \bar{\theta}^* e^{-i\phi^*} \\
& - \sqrt{B_L B_T} \sin \frac{\theta}{2} \cos \frac{\bar{\theta}}{2} \sin \theta^* \frac{1 - \cos \bar{\theta}^*}{\sqrt{2}} e^{i\bar{\phi}^*} \\
& \left. - B_T \cos \frac{\theta}{2} \cos \frac{\bar{\theta}}{2} \frac{(1 - \cos \theta^*)(1 - \cos \bar{\theta}^*)}{2} e^{-i(\phi^* - \bar{\phi}^*)} \right\} \\
+ & \mathcal{M}_{\lambda_1 \lambda_2}^{RR}(\Theta) \left\{ -B_L \cos \frac{\theta}{2} \cos \frac{\bar{\theta}}{2} e^{i(\phi - \bar{\phi})} \sin \theta^* \sin \bar{\theta}^* \right. \\
& + \sqrt{B_L B_T} \sin \frac{\theta}{2} \cos \frac{\bar{\theta}}{2} e^{i(\phi - \bar{\phi})} \frac{1 - \cos \theta^*}{\sqrt{2}} \sin \bar{\theta}^* e^{-i\phi^*} \\
& + \sqrt{B_L B_T} \cos \frac{\theta}{2} \sin \frac{\bar{\theta}}{2} e^{i(\phi - \bar{\phi})} \sin \theta^* \frac{1 - \cos \bar{\theta}^*}{\sqrt{2}} e^{i\bar{\phi}^*} \\
& \left. - B_T \sin \frac{\theta}{2} \sin \frac{\bar{\theta}}{2} e^{i(\phi - \bar{\phi})} \frac{(1 - \cos \theta^*)(1 - \cos \bar{\theta}^*)}{2} e^{-i(\phi^* - \bar{\phi}^*)} \right\} \\
+ & \mathcal{M}_{\lambda_1 \lambda_2}^{LR}(\Theta) \left\{ -B_L \sin \frac{\theta}{2} \cos \frac{\bar{\theta}}{2} e^{-i\bar{\phi}} \sin \theta^* \sin \bar{\theta}^* \right.
\end{aligned}$$

$$\begin{aligned}
& - \sqrt{B_L B_T} \cos \frac{\theta}{2} \cos \frac{\bar{\theta}}{2} e^{-i\bar{\phi}} \frac{1 - \cos \theta^*}{\sqrt{2}} \sin \bar{\theta}^* e^{-i\phi^*} \\
& + \sqrt{B_L B_T} \sin \frac{\theta}{2} \sin \frac{\bar{\theta}}{2} e^{-i\bar{\phi}} \sin \theta^* \frac{1 - \cos \bar{\theta}^*}{\sqrt{2}} e^{i\bar{\phi}^*} \\
& + B_T \cos \frac{\theta}{2} \sin \frac{\bar{\theta}}{2} e^{-i\bar{\phi}} \frac{(1 - \cos \theta^*)(1 - \cos \bar{\theta}^*)}{2} e^{-i(\phi^* - \bar{\phi}^*)} \} \\
+ \mathcal{M}_{\lambda_1 \lambda_2}^{RL}(\Theta) & \{ - B_L \cos \frac{\theta}{2} \sin \frac{\bar{\theta}}{2} e^{i\phi} \sin \theta^* \sin \bar{\theta}^* \\
& + \sqrt{B_L B_T} \sin \frac{\theta}{2} \sin \frac{\bar{\theta}}{2} e^{i\phi} \frac{1 - \cos \theta^*}{\sqrt{2}} \sin \bar{\theta}^* e^{-i\phi^*} \\
& - \sqrt{B_L B_T} \cos \frac{\theta}{2} \cos \frac{\bar{\theta}}{2} e^{i\phi} \sin \theta^* \frac{1 - \cos \bar{\theta}^*}{\sqrt{2}} e^{i\bar{\phi}^*} \\
& + B_T \sin \frac{\theta}{2} \cos \frac{\bar{\theta}}{2} e^{i\phi} \frac{(1 - \cos \theta^*)(1 - \cos \bar{\theta}^*)}{2} e^{-i(\phi^* - \bar{\phi}^*)} \}.
\end{aligned}$$

The differential cross section of eq. (3.8) is now expressed in terms of the $\gamma\gamma \rightarrow t\bar{t}$ amplitudes $\mathcal{M}_{\lambda_1 \lambda_2}^{\sigma\bar{\sigma}}(\Theta)$.

B Cross section for the process $\gamma\gamma \rightarrow t\bar{t} \rightarrow bW^+ \bar{b}W^-$

By using the W^+ and W^- decay angular distributions of eq. (3.8) and the appendix A, one can project out the polarized W^+W^- production cross sections. The cross section for the process $\gamma(\lambda_1)\gamma(\lambda_2) \rightarrow t\bar{t} \rightarrow bW^+(\Lambda)\bar{b}W^-(\bar{\Lambda})$ is expressed as

$$\frac{d\hat{\sigma}_{\lambda_1 \lambda_2}}{d \cos \Theta d \cos \theta d \phi d \cos \bar{\theta} d \bar{\phi}} = \frac{\beta}{32\pi \hat{s}} \sum_{\Lambda=0,-} \sum_{\bar{\Lambda}=0,+} |\mathbf{M}_{\lambda_1 \lambda_2}^{\Lambda \bar{\Lambda}}(\Theta; \theta, \phi, \bar{\theta}, \bar{\phi})|^2, \quad (\text{B.1})$$

where

$$\begin{aligned}
|\mathbf{M}_{\lambda_1 \lambda_2}^{\Lambda \bar{\Lambda}}(\Theta; \theta, \phi, \bar{\theta}, \bar{\phi})|^2 &= |\mathcal{M}_{\lambda_1 \lambda_2}^{RR}|^2 |D_R^\Lambda|^2 |\bar{D}_R^{\bar{\Lambda}}|^2 \\
&+ |\mathcal{M}_{\lambda_1 \lambda_2}^{LL}|^2 |D_L^\Lambda|^2 |\bar{D}_L^{\bar{\Lambda}}|^2 \\
&+ |\mathcal{M}_{\lambda_1 \lambda_2}^{RL}|^2 |D_R^\Lambda|^2 |\bar{D}_L^{\bar{\Lambda}}|^2 \\
&+ |\mathcal{M}_{\lambda_1 \lambda_2}^{LR}|^2 |D_L^\Lambda|^2 |\bar{D}_R^{\bar{\Lambda}}|^2 \\
&+ 2 \text{Re} [\mathcal{M}_{\lambda_1 \lambda_2}^{RR} \cdot \mathcal{M}_{\lambda_1 \lambda_2}^{LL*}] \text{Re} [D_R^\Lambda \bar{D}_R^{\bar{\Lambda}} D_L^{\Lambda*} \bar{D}_L^{\bar{\Lambda}*}]
\end{aligned} \quad (\text{B.2})$$

$$\begin{aligned}
& - 2 \operatorname{Im} \left[\mathcal{M}_{\lambda_1 \lambda_2}^{RR} \cdot \mathcal{M}_{\lambda_1 \lambda_2}^{LL*} \right] \operatorname{Im} \left[D_R^\Lambda \bar{D}_R^\Lambda D_L^{\Lambda*} \bar{D}_L^{\Lambda*} \right] \\
& + 2 \operatorname{Re} \left[\mathcal{M}_{\lambda_1 \lambda_2}^{RR} \cdot \mathcal{M}_{\lambda_1 \lambda_2}^{RL*} \right] \operatorname{Re} \left[D_R^\Lambda \bar{D}_R^\Lambda D_R^{\Lambda*} \bar{D}_L^{\Lambda*} \right] \\
& - 2 \operatorname{Im} \left[\mathcal{M}_{\lambda_1 \lambda_2}^{RR} \cdot \mathcal{M}_{\lambda_1 \lambda_2}^{RL*} \right] \operatorname{Im} \left[D_R^\Lambda \bar{D}_R^\Lambda D_R^{\Lambda*} \bar{D}_L^{\Lambda*} \right] \\
& + 2 \operatorname{Re} \left[\mathcal{M}_{\lambda_1 \lambda_2}^{RR} \cdot \mathcal{M}_{\lambda_1 \lambda_2}^{LR*} \right] \operatorname{Re} \left[D_R^\Lambda \bar{D}_R^\Lambda D_L^{\Lambda*} \bar{D}_R^{\Lambda*} \right] \\
& - 2 \operatorname{Im} \left[\mathcal{M}_{\lambda_1 \lambda_2}^{RR} \cdot \mathcal{M}_{\lambda_1 \lambda_2}^{LR*} \right] \operatorname{Im} \left[D_R^\Lambda \bar{D}_R^\Lambda D_L^{\Lambda*} \bar{D}_R^{\Lambda*} \right] \\
& + 2 \operatorname{Re} \left[\mathcal{M}_{\lambda_1 \lambda_2}^{LL} \cdot \mathcal{M}_{\lambda_1 \lambda_2}^{RL*} \right] \operatorname{Re} \left[D_L^\Lambda \bar{D}_L^\Lambda D_R^{\Lambda*} \bar{D}_L^{\Lambda*} \right] \\
& - 2 \operatorname{Im} \left[\mathcal{M}_{\lambda_1 \lambda_2}^{LL} \cdot \mathcal{M}_{\lambda_1 \lambda_2}^{RL*} \right] \operatorname{Im} \left[D_L^\Lambda \bar{D}_L^\Lambda D_R^{\Lambda*} \bar{D}_L^{\Lambda*} \right] \\
& + 2 \operatorname{Re} \left[\mathcal{M}_{\lambda_1 \lambda_2}^{LL} \cdot \mathcal{M}_{\lambda_1 \lambda_2}^{LR*} \right] \operatorname{Re} \left[D_L^\Lambda \bar{D}_L^\Lambda D_L^{\Lambda*} \bar{D}_R^{\Lambda*} \right] \\
& - 2 \operatorname{Im} \left[\mathcal{M}_{\lambda_1 \lambda_2}^{LL} \cdot \mathcal{M}_{\lambda_1 \lambda_2}^{LR*} \right] \operatorname{Im} \left[D_L^\Lambda \bar{D}_L^\Lambda D_L^{\Lambda*} \bar{D}_R^{\Lambda*} \right] \\
& + 2 \operatorname{Re} \left[\mathcal{M}_{\lambda_1 \lambda_2}^{RL} \cdot \mathcal{M}_{\lambda_1 \lambda_2}^{LR*} \right] \operatorname{Re} \left[D_R^\Lambda \bar{D}_L^\Lambda D_L^{\Lambda*} \bar{D}_R^{\Lambda*} \right].
\end{aligned}$$

It is helpful to write down the squared amplitudes in the case where $\lambda_1 = \lambda_2 = \lambda$, because high luminosity and high degree of $\lambda_1 = \lambda_2 = \lambda$ polarization for energetic two photon pairs can be achieved at a PLC by choosing a right combination of the laser and the e^- beam polarizations. We find

$$\begin{aligned}
|\mathbf{M}_{\lambda\lambda}^{00}|^2 &= \left\{ |\mathcal{M}_{\lambda\lambda}^{RR}|^2 \cos^2 \frac{\theta}{2} \cos^2 \frac{\bar{\theta}}{2} + |\mathcal{M}_{\lambda\lambda}^{LL}|^2 \sin^2 \frac{\theta}{2} \sin^2 \frac{\bar{\theta}}{2} \right. \\
&\quad + \frac{1}{2} \operatorname{Re}[\mathcal{M}_{\lambda\lambda}^{RR} \cdot \mathcal{M}_{\lambda\lambda}^{LL*}] \sin \theta \sin \bar{\theta} \cos(\phi - \bar{\phi}) \\
&\quad \left. - \frac{1}{2} \operatorname{Im}[\mathcal{M}_{\lambda\lambda}^{RR} \cdot \mathcal{M}_{\lambda\lambda}^{LL*}] \sin \theta \sin \bar{\theta} \sin(\phi - \bar{\phi}) \right\} \times \frac{B_L^2}{4\pi^2}, \\
|\mathbf{M}_{\lambda\lambda}^{0+}|^2 &= \left\{ |\mathcal{M}_{\lambda\lambda}^{RR}|^2 \cos^2 \frac{\theta}{2} \sin^2 \frac{\bar{\theta}}{2} + |\mathcal{M}_{\lambda\lambda}^{LL}|^2 \sin^2 \frac{\theta}{2} \cos^2 \frac{\bar{\theta}}{2} \right. \\
&\quad - \frac{1}{2} \operatorname{Re}[\mathcal{M}_{\lambda\lambda}^{RR} \cdot \mathcal{M}_{\lambda\lambda}^{LL*}] \sin \theta \sin \bar{\theta} \cos(\phi - \bar{\phi}) \\
&\quad \left. + \frac{1}{2} \operatorname{Im}[\mathcal{M}_{\lambda\lambda}^{RR} \cdot \mathcal{M}_{\lambda\lambda}^{LL*}] \sin \theta \sin \bar{\theta} \sin(\phi - \bar{\phi}) \right\} \times \frac{B_L B_T}{4\pi^2}, \\
|\mathbf{M}_{\lambda\lambda}^{-0}|^2 &= \left\{ |\mathcal{M}_{\lambda\lambda}^{RR}|^2 \sin^2 \frac{\theta}{2} \cos^2 \frac{\bar{\theta}}{2} + |\mathcal{M}_{\lambda\lambda}^{LL}|^2 \cos^2 \frac{\theta}{2} \sin^2 \frac{\bar{\theta}}{2} \right. \\
&\quad \left. - \frac{1}{2} \operatorname{Re}[\mathcal{M}_{\lambda\lambda}^{RR} \cdot \mathcal{M}_{\lambda\lambda}^{LL*}] \sin \theta \sin \bar{\theta} \cos(\phi - \bar{\phi}) \right\}
\end{aligned} \tag{B.3}$$

$$\begin{aligned}
& + \frac{1}{2} \operatorname{Im}[\mathcal{M}_{\lambda\lambda}^{RR} \cdot \mathcal{M}_{\lambda\lambda}^{LL*}] \sin \theta \sin \bar{\theta} \sin(\phi - \bar{\phi}) \} \times \frac{B_L B_T}{4\pi^2}, \\
|\mathbf{M}_{\lambda\lambda}^{-+}|^2 = & \{ |\mathcal{M}_{\lambda\lambda}^{RR}|^2 \sin^2 \frac{\theta}{2} \sin^2 \frac{\bar{\theta}}{2} + |\mathcal{M}_{\lambda\lambda}^{LL}|^2 \cos^2 \frac{\theta}{2} \cos^2 \frac{\bar{\theta}}{2} \\
& + \frac{1}{2} \operatorname{Re}[\mathcal{M}_{\lambda\lambda}^{RR} \cdot \mathcal{M}_{\lambda\lambda}^{LL*}] \sin \theta \sin \bar{\theta} \cos(\phi - \bar{\phi}) \\
& - \frac{1}{2} \operatorname{Im}[\mathcal{M}_{\lambda\lambda}^{RR} \cdot \mathcal{M}_{\lambda\lambda}^{LL*}] \sin \theta \sin \bar{\theta} \sin(\phi - \bar{\phi}) \} \times \frac{B_T^2}{4\pi^2}.
\end{aligned}$$

References

- [1] K. Abe et al., [ACFA Linear Collider Working Group Collaboration], ‘Particle Physics Experiments at JLC’, hep-ph/0109166.
- [2] J. Aguilar-Saavedra et al., [ECFA/DESY LC Physics Working Group Collaboration], ‘Physics at an e^+e^- Linear Collider’, hep-ph/0106315.
- [3] T. Abe et al., [American Linear Collider Working Group Collaboration], in *Proc. of the APS/DPF/DPB Summer Study on the Future of Particle Physics (Snowmass 2001)* ed. R. Davidson and C. Quigg, SLAC-R-570 *Resource book for Snowmass 2001, 30 Jun - 21 Jul 2001, Snowmass, Colorado*.
- [4] I.F. Ginzburg, G.L. Kotkin, S.L. Panfil, V.G. Selbo and V.I. Telnov, *Nucl. Instrum. Methods Phys. Res.* **A219**, 5 (1984);
V.I. Telnov, *ibid.* **294**, 72 (1990).
- [5] M.M. Muhlleitner, M. Kramer, M. Spira and P.M. Zerwas, *Phys. Lett.* **B508**, 311 (2001);
D.M. Asner, J.B. Gronberg and J.F. Gunion, *Phys. Rev.* **D67**, 035009 (2003).
- [6] G.V. Jikia, *Nucl. Phys.* **B405**, 24 (1993);
M.S. Berger, *Phys. Rev.* **D48**, 5121 (1993);
T. Ohgaki, T. Takahashi and I. Watanabe, *Phys. Rev.* **D56**, 1723 (1997);
G. Jikia and S. Soldner-Rembold, *Nucl. Instrum. Meth.* **A472**, 133 (2001);
P. Niezurawski, A.F. Zarnecki and M. Krawczyk, hep-ph/0207294.
- [7] B. Grazadkowski and J.F. Gunion, *Phys. Lett.* **B294**, 361 (1992);
M. Kramer, J. Kühn, M.L. Stong and P.M. Zerwas, *Z. Phys.* **C64**, 21 (1994);
J.F. Gunion and J.G. Kelly, *Phys. Lett.* **B333**, 110 (1994).
- [8] K. Hagiwara, *Nucl. Instrum. Meth.* **A472**, 12 (2001).

- [9] E. Asakawa, J. Kamoshita, A. Sugamoto and I. Watanabe, *Eur. Phys. J.* **C14**, 335 (2000).
- [10] E. Asakawa, S.Y. Choi, K. Hagiwara and J.S. Lee, *Phys. Rev.* **D62**, 115005 (2000).
- [11] R.M. Godbole, S.D. Rindani and R.K. Singh, *Phys. Rev.* **D67**, 095009 (2003).
- [12] K. Hagiwara and D. Zeppenfeld, *Nucl. Phys.* **B274**, 1 (1986).
- [13] J.F. Gunion, H.E. Haber, G. Kane, S. Dawson, Higgs hunter's guide (Addison-Wesley Publishing Company 1990) , and references therein.
- [14] E. Asakawa and K. Hagiwara, in preparation
- [15] K. Hagiwara, H. Murayama and I. Watanabe, *Nucl. Phys.* **B367**, 257 (1991).
- [16] M. Jezabek and J.H. Kühn, *Nucl. Phys.* **B320**, 20 (1989);
G. Mahlon and S. Parke, *Phys. Rev.* **D53**, 4886 (1996).
- [17] M. Diehl and O. Nachtman, *Z. Phys.* **C62**, 397 (1994);
J.F. Gunion, B. Grzadkowski and X.-G. He, *Phys. Rev. Lett.* **77**, 5172 (1996);
K. Hagiwara, S. Ishihara, J. Kamoshita and B.A. Kniehl, *Eur. Phys. J.* **C14**, 457 (2000).
- [18] A. Djouadi, J. Kalinowski and M. Spira, *Comm. Phys. Commun. Res.* **108**, 56 (1998).
- [19] H. Murayama, I. Watanabe and K. Hagiwara, HELAS: HELicity Amplitude Subroutines for Feynman Diagram Evaluations, KEK Report 91-11 (1992).